

Efficacy of early stellar feedback in low gas surface density environments

Rahul Kannan^{1*†}, Federico Marinacci¹, Christine M. Simpson^{2,3,4}, Simon C. O. Glover⁵ and Lars Hernquist¹

¹Harvard-Smithsonian Center for Astrophysics, 60 Garden Street, Cambridge 02138, MA, USA

²Heidelberg Institute for Theoretical Studies, Schloss- Wolfsbrunnenweg 35, D-69118 Heidelberg, Germany

³Enrico Fermi Institute, University of Chicago, Chicago, IL 60637, USA

⁴Department of Astronomy & Astrophysics, University of Chicago, Chicago, IL 60637, USA

⁵Universität Heidelberg, Zentrum für Astronomie, Institut für theoretische Astrophysik, Albert-Ueberle-Str. 2, 69120 Heidelberg, Germany

Accepted XXX. Received YYY; in original form ZZZ

ABSTRACT

We present a suite of high resolution radiation hydrodynamic simulations of a small patch (1 kpc²) of the inter-stellar medium (ISM) performed with AREPO-RT, with the aim to quantify the efficacy of various feedback processes like supernovae explosions (SNe), photoheating and radiation pressure in low gas surface density galaxies ($\Sigma_{\text{gas}} \simeq 10 M_{\odot} \text{ pc}^{-2}$). We show that radiation fields decrease the star formation rate and therefore the total stellar mass formed by a factor of ~ 2 . This increases the gas depletion timescale and brings the simulated Kennicutt-Schmidt relation closer to the observational estimates. Radiation feedback coupled with SNe is more efficient at driving outflows with the mass and energy loading increasing by a factor of ~ 10 . This increase is mainly driven by the additional entrainment of medium density ($10^{-2} \leq n < 1 \text{ cm}^{-3}$), warm ($300 \text{ K} \leq T < 8000 \text{ K}$) material. Therefore including radiation fields tends to launch colder, denser and higher mass and energy loaded outflows. This is because photoheating of the high density gas around a newly formed star over-pressurises the region, causing it to expand. This reduces the ambient density in which the SNe explode by a factor of 10 – 100 which in turn increases their momentum output by a factor of $\sim 1.5 - 2.5$. Finally, we note that in these low gas surface density environments, radiation fields primarily impact the ISM via photoheating and radiation pressure has only a minimal role in regulating star formation.

Key words: radiative transfer – radiation: dynamics – methods: numerical – ISM: structure – galaxies: ISM

1 INTRODUCTION

Stellar feedback has been invoked by many models to explain the low efficiency of star formation in low mass ($M_{\text{halo}} \lesssim 10^{12} M_{\odot}$) haloes (Navarro et al. 1996; Springel & Hernquist 2003; Stinson et al. 2006; Dalla Vecchia & Schaye 2008; Agertz et al. 2013; Vogelsberger et al. 2013; Hopkins et al. 2014, 2017). Early cosmological simulations invoked the energy injection from SNe events as the main feedback mechanism to regulate star formation. However, the lack of resolution meant that the coupling between supernovae (SNe) feedback energy and the ISM was very inefficient (Katz et al. 1996; Navarro et al. 1996), as most of the injected energy is radiated away quite quickly. This precipitated the need to treat SNe feedback on sub-grid scales, which involved models such as de-

layed cooling of gas heated by a SNe event (Thacker & Couchman 2001; Stinson et al. 2006; Agertz et al. 2013), stochastic heating of the gas to temperatures where cooling becomes inefficient (Dalla Vecchia & Schaye 2008; Schaye et al. 2015) and injecting kinetic energy that adds velocity kicks to gas particles to remove them from the inner regions of galactic discs (Springel & Hernquist 2003; Oppenheimer & Davé 2006; Vogelsberger et al. 2013). These models have been quite successful in reproducing the properties of galaxies in a broad sense (Vogelsberger et al. 2014a,b; Schaye et al. 2015; Springel et al. 2018; Marinacci et al. 2018; Naiman et al. 2018; Nelson et al. 2018; Pillepich et al. 2018). However, they require the fine tuning of quite a few number of free parameters that do not necessarily map to a set of physical processes. In many cases they also require unrealistic values of SNe feedback energy ($> 10^{51}$ erg; Guedes et al. 2011; Schaye et al. 2015) or excessively large gas outflow velocities (Pillepich et al. 2018).

Only recently has there been a push to quantify the momen-

* E-mail: rahul.kannan@cfa.harvard.edu

† Einstein Fellow

tum input of SNe events by performing high resolution simulations that resolve the cooling radius and the Sedov-taylor phase of the explosion (Kim & Ostriker 2015; Martizzi et al. 2015; Walch & Naab 2015; Haid et al. 2016), which showed that the momentum amplification that can be achieved is of the order of $\sim 13 - 30$. However, even with the momentum boost included, SNe feedback alone is not able to regulate star formation in galaxies (Girichidis et al. 2016), if the stars are assumed to form and explode in the high density peaks of the ISM. Only for random SNe positions is the energy injected in sufficiently low-density environments to reduce energy losses significantly. It enhances the effective coupling between the SNe feedback energy and the ISM leading to more realistic velocity dispersions and strong, high mass loaded winds leading to a global regulation of star formation. Similar results have been found by Kim & Ostriker (2017), who showed the importance of binary stars that leave their birth cloud and are able to deposit energy in lower density environments.

In addition to SNe, young massive stars deposit large amounts of energy in the form of photons and stellar winds, which can have a significant dynamical impact on the ISM (Leitherer et al. 1999; Murray et al. 2010; Walch et al. 2012; Agertz et al. 2013). Stinson et al. (2013) showed that the high energy photons emitted by O and B stars can ionize and photoheat the surrounding regions, thereby preprocessing the sites of SNe explosions. This helps regulate star formation especially at high redshifts (Kannan et al. 2014b). This required full thermalization of the injected UV radiation energy close to the source, which is not guaranteed as most of the energy of the photons is utilized to photoionize the gas. Radiation pressure, both direct UV and multiscattered infrared (IR), is another mechanism invoked to drive significant outflows ($\sim 100 \text{ km s}^{-1}$) (Hopkins et al. 2011; Agertz et al. 2013; Hopkins et al. 2014). It is however, unclear whether the gas can actually trap the photons efficiently. Krumholz & Thompson (2013) using a Flux Limited Diffusion (FLD) RT scheme, showed that as the gas accelerates in the presence of the gravitational potential of the disc, it becomes Rayleigh-Taylor unstable, creating channels through which photons escape, reducing the efficacy of this mechanism. Simulations performed with more accurate RT algorithms disagree with the previous calculations and show that it is indeed possible to drive outflows even when the gas becomes Rayleigh-Taylor unstable (Davis et al. 2014; Zhang & Davis 2017). In any case, large optical depths ($\tau_{\text{IR}} \sim 50$) are required to effectively trap the photons and boost the momentum injection to the levels required to efficiently suppress star formation (Roškar et al. 2014). These conditions are currently thought to only exist in galaxies with extremely high gas surface densities $\Sigma_{\text{gas}} \gtrsim 200 \text{ M}_{\odot} \text{ pc}^{-2}$. Alternatively, if enough radiation escapes the star forming regions and the ISM of galaxies, it can in principle reduce the gas cooling rates of the circum-galactic medium (CGM) thereby reducing gas inflows into the centers of galaxies (Cantalupo 2010; Gnedin & Hollon 2012; Kannan et al. 2014a, 2016).

While these works hint towards the importance of radiation fields, the crude nature of these sub-grid models makes it difficult to gauge the exact mechanisms and significance of radiation fields in regulating the star formation rates of low mass galaxies. Therefore, full radiation hydrodynamic simulations are necessary in order to gain a fundamental understanding of stellar feedback (Rosdahl et al. 2015; Kim & Ostriker 2017; Peters et al. 2017; Emmerich et al. 2018). Rosdahl et al. (2015) using radiation hydrodynamic (RHD) isolated disc simulations showed that photoheating suppresses star formation by making the disc smooth and thick and by preventing of the formation of dense clouds (rather than dis-

persing them). Radiation pressure (both UV and multi-scattering IR) was shown to be unimportant. The need to simulate the entire disc necessitated relatively low resolutions ($\sim 20 - 30 \text{ pc}$), which meant that both the Strömgren radius around young massive stars and the Sedov-Taylor phase of the SNe explosion were only partially resolved. Peters et al. (2017) showed that radiation fields in combination with stellar winds can regulate star formation in solar-neighbourhood like environments. However, the effect of radiation pressure was left unexplored.

In this paper, we perform high resolution ($\Delta x \sim 0.45 \text{ pc}$; $M_{\text{gas}} = 10 \text{ M}_{\odot}$) simulations of a patch of the ISM to investigate and quantify the role of various stellar feedback processes like SNe, photoheating and radiation pressure (both UV and Multi-scattered IR) in low gas surface density galaxies. These high resolutions ensure that the relevant spatial and mass scales are sufficiently resolved, thereby providing an accurate picture of stellar feedback. The paper is structured as follows. In Section 2 we outline the simulations performed. Section 3 describes the results obtained. The interpretation of the results is presented in Section 4 and finally, we present our conclusions in Section 5.

2 METHODS

Our simulation setup is the same as the one described in Simpson et al. (2016) which in turn is based on the setup described in Creasey et al. (2013). Briefly it consists of a column of stratified gas intended to represent a small portion of a galactic disk. The domain dimensions are $1 \times 1 \times 10 \text{ kpc}$ and we impose periodic boundaries along the two short (x & y) axes and outflow boundaries along the long (z) axis. The gravitational forces are computed as a sum of self-gravity and an external potential mimicking the pre-existing stellar density field. The self-gravity is computed using a tree based algorithm. An adaptive softening is used for gas cells with a minimum value of $\epsilon_{\text{gas}} = 0.165 \text{ pc}$. The collisionless stellar particles have a fixed softening of $\epsilon_{\text{star}} = 0.165 \text{ pc}$. The stellar density field is proportional to the initial gas density ($\rho_{\text{gas},0}$) field via the assumed gas fraction (f_g); $\rho_{\star} = \rho_{\text{gas},0}(f_g^{-1} - 1)$. The initial gas density profile is given by

$$\rho_{\text{gas},0} = \frac{\Sigma_0}{2b_0} \text{sech}^2\left(\frac{h}{b_0}\right), \quad (1)$$

where the gas surface density is set to $\Sigma_0 = 10 \text{ M}_{\odot} \text{ pc}^{-2}$, the scale height is $b_0 = 100 \text{ pc}$ and the gas fraction is $f_g = 0.1$. Note that the gas fraction is smaller than the fiducial value of the solar neighbourhood ($f_g \simeq 0.25$), and the inverse correlation between the stellar potential and the gas fraction means that our gravitational potential is a factor of 2.5 larger than solar neighbourhood conditions. This has important implications for the star formation rates obtained in our simulations (see Section 3 for more details). We impose a minimum density threshold of $10^{-20} \text{ M}_{\odot} \text{ pc}^{-3}$.

The simulations are performed with AREPO-RT (Kannan et al. 2018) a radiation hydrodynamic extension to the moving mesh code AREPO (Springel 2010; Pakmor et al. 2016). AREPO provides a quasi-lagrangian solution to the hydrodynamic equations by solving them at interfaces between moving mesh cells in the rest frame of the interface. We assume a thermal adiabatic index of $\gamma = 5/3$. A minimum allowed temperature of 5 K is adopted. The initial setup consists of 10^6 gas cells, concentrated in the mid-plane, but also comprising a Cartesian background mesh with a cell length of 43.5 pc up to 1 kpc and of 90.9 pc beyond. Refinement

and derefinement of the mesh is applied to maintain roughly constant cell masses to within a factor of two of the target gas mass of $10 M_{\odot}$, subject to the constraints that cell volumes are approximately limited between 0.1 pc^3 and $7.19 \times 10^5 \text{ pc}^3$, a maximum volume ratio of 8 between adjacent cells is maintained, and cell diameters are required to be no larger than $1/4$ of the Jeans length. To keep the Jeans length resolved after gravitational collapse has reached the minimum allowed cell volume, an effective pressure floor in the Riemann solver equal to 4^2 times the Jeans pressure is imposed (Machacek et al. 2001).

The RHD module solves the moment-based radiative transfer equations using the M1 closure relation. We achieve second order accuracy by using a slope-limited linear spatial extrapolation and a first order time prediction step to obtain the values of the primitive variables on both sides of the cell interface, which are then used to solve the Riemann problem at the interface. This allows the code to be extremely accurate and have excellent diffusivity control. The M1 closure method is fully local in nature, such that the computational cost is independent of the number of sources and only depends on the number of resolution elements in the simulation.

We use the chemistry and cooling network outlined in Smith et al. (2014). It solves the hydrogen chemistry, including H_2 (Glover & Mac Low 2007a,b) and has a simple treatment for CO chemistry (Nelson & Langer 1997; Glover & Clark 2012). The carbon, oxygen and helium abundances are the same as used in Smith et al. (2014). The dust to gas ratio is assumed to be $f_d = 0.01$. We do not use any external radiation field as they will be generated self-consistently in our simulations. Metal cooling of high-temperature gas assuming collisional ionization equilibrium is also included (Gnat & Ferland 2012; Walch & Naab 2015) assuming a constant solar gas metallicity.

The chemistry network is coupled to radiation fields using a multi-frequency approach. We use six frequency bins: the IR band ($0.1 - 1 \text{ eV}$), optical band ($1 - 11.2 \text{ eV}$), the Lyman-Werner (LW; H_2 dissociation) band ($11.2 - 13.6 \text{ eV}$), hydrogen ionization band ($13.6 - 15.2 \text{ eV}$), H and H_2 ionization band ($15.2 - 24.6 \text{ eV}$) and finally the He ionization band ($24.6 - 100.0 \text{ eV}$). The dust opacity to IR radiation is set to $\kappa_{\text{IR}} = 10 \text{ cm}^2 \text{ g}^{-1}$ and the opacity for all other radiation bins is $\kappa_{\text{UV}} = 1000 \text{ cm}^2 \text{ g}^{-1}$. The photoionization and photoheating rates for each bin are calculated as described in Section 3.2.1 of Kannan et al. (2018).

Accurately simulating H_2 thermochemistry is quite tricky as only about 10% of the LW absorption leads to dissociation and the rest of the photons are destroyed without contributing to photodissociation (Draine & Bertoldi 1996; Sternberg et al. 2014). The absorption rate is highly dependent on the wavelength of the LW band (Haiman et al. 2000) because more resonant bands become optically thick at high H_2 column densities, and dissociation is quashed, while bands with weaker absorption can still penetrate the cloud. Hence, H_2 self-shielding functions calculated from experiments are given in terms of the column density of H_2 (Gnedin & Draine 2014). Unfortunately, our formulation of the RT equations does not track the optical depth of individual rays. Therefore, we resort to using the method described in Nickerson et al. (2018) and boost the destruction of LW photons by a constant factor to incorporate the fact that only a fraction of LW photon absorption leads to H_2 dissociation. As the LW photons propagate through gas cells, their repeated destruction mimics the column density variation of H_2 destruction rates. A test for this scheme is presented in Appendix A.

Stars are formed following a standard stochastic approach.

The density threshold for star formation is set to $n = 100 \text{ cm}^{-3}$. The star formation rate of a cell ‘i’ above this threshold is set to

$$\text{sfr}_i = \epsilon_{\text{ff}} \frac{m_i}{t_{\text{ff}}}, \quad (2)$$

where ϵ_{ff} is the star formation efficiency per free fall time of gas (set to 0.02) and t_{ff} is the free fall time of the gas defined as

$$t_{\text{ff}} = \sqrt{\frac{3\pi}{32G\rho_i}}. \quad (3)$$

The probability of a cell forming a star is then given by

$$p_i = \text{sfr}_i \frac{\Delta t}{m_*}, \quad \text{where } m_* = \min\{m_i, m_{\text{max}}\}. \quad (4)$$

Collisionless particles of mass m_* , representing stellar populations, are formed stochastically from the gas, with the probability of forming one drawn from a Poisson distribution. Note that if $m_i = m_*$, then the whole cell is converted to stars else part of the cell mass is converted into stars with the the maximum stellar mass set to $m_{\text{max}} = 20 M_{\odot}$.

We assume a Chabrier (Chabrier 2003) stellar initial mass function (IMF). Stars with initial mass $M_* \geq 8 M_{\odot}$ are assumed to explode as SNe at the end of their lifetime. This sets the SNe rate $\text{SNR} \sim 1$ per $100 M_{\odot}$ of stars formed. The extremely high mass resolution of our simulations necessitates the need for a probabilistic approach to stellar feedback. As soon as a star is formed we tag that stellar particle to go SNe in a probabilistic manner. The probability of a star going SNe is given as

$$p_{\text{SNe}} = \text{SNR} \frac{m_*}{100 M_{\odot}}. \quad (5)$$

We then enforce that only the tagged SNe particles emit radiation fields. This ensures that irrespective of the mass of the stellar particle, it emits radiation equivalent to $100 M_{\odot}$ of new stars formed. The radiation luminosity and spectra are obtained from Bruzual & Charlot (2003). The time delay between star formation and the SNe event is set to 5 Myr. We assume that the stars only emit radiation during this time and as soon as they go SNe their radiation output stops. This is a good approximation as stellar population synthesis models predict a precipitous drop in the radiation output after about 3 Myr, when the most massive stars start to die off. SNe are modeled as discrete explosions of 10^{51} erg deposited as purely thermal energy into the 32 closest cells to the explosion position. Explosion events are only added to the mesh when all gas cells are synchronized; the maximum allowed timestep is 0.1 Myr. The high mass and spatial resolution of our simulations ensures that the right momentum boost is recovered (Simpson et al. 2015, 2016).

The amount of UV ionizing photons per $100 M_{\odot}$ of stars formed is about $\dot{N}_{\gamma} = 5 \times 10^{48}$ photons s^{-1} (Bruzual & Charlot 2003). The Strömgren radius (r_s), assuming full ionization within r_s , is given by

$$r_s = \left(\frac{3\dot{N}_{\gamma}}{4\pi\alpha_B n_{\text{H}}^2} \right)^{1/3}, \quad (6)$$

where $\alpha_B = 2.63 \times 10^{-13} \text{ cm}^3 \text{ s}^{-1}$ is the Case B recombination rate for hydrogen atoms at $T = 10^4 \text{ K}$. The minimum cell sizes in our simulation reaches about 0.1 pc^3 which equates to maximum density at which the Strömgren radius is resolvable to $n = 2.6 \times 10^3 \text{ cm}^{-3}$. Above this density r_s will be unresolved and the effect of photoheating will be underestimated. To increase the probability of resolving the r_s , we inject all the photons in the cell closest to the star particle. Additionally, the direction of the photon flux (\mathbf{F}_r) is set to be radially outward from the star particle and the

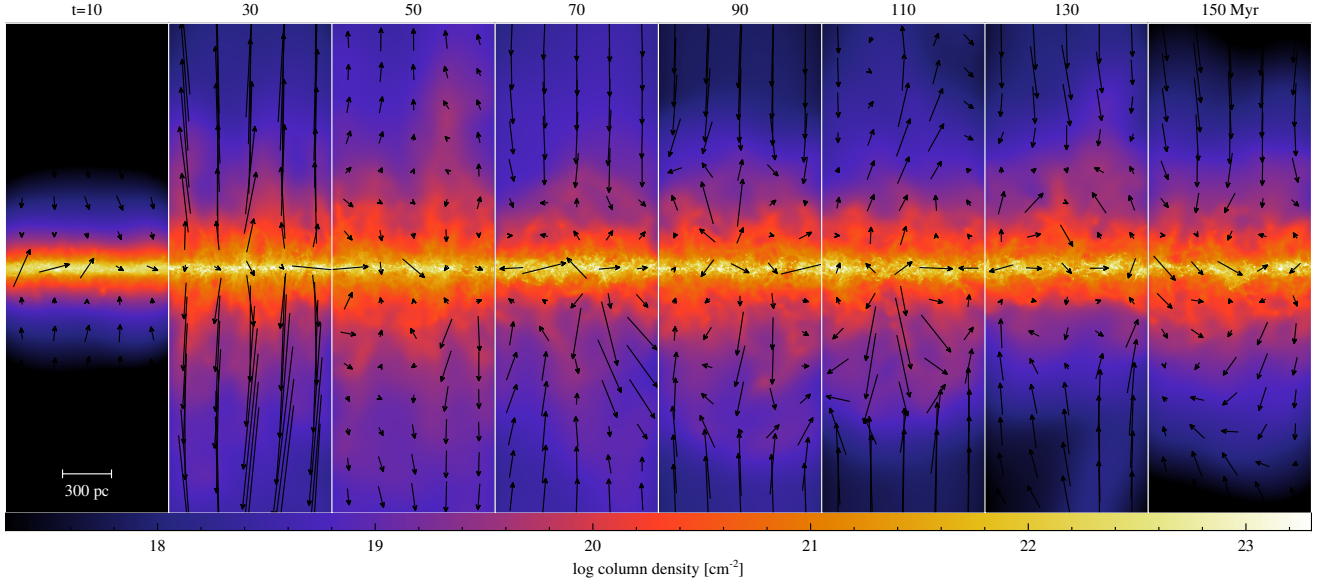


Figure 1. Map of the column density along the line of sight in the SN simulation at $t = 10$ (first column), 30 (second column), 50 (third column), 70 (fourth column), 90 (fifth column), 110 (sixth column), 130 (seventh column) and 150 (eighth column) Myr. The dimensions of the box shown in the image are 1×3 kpc. The black arrows indicate the direction of the velocity field with the length of the arrows indicating the magnitude of the velocity field. The initial starburst drives large scale ($\sim 3 - 4$ kpc) outflows ($t = 30 - 50$ Myr), followed by a period of infall ($t = 50 - 70$ Myr), after which the disc settles down with a small scale fountain flow (\lesssim kpc) operating from $t = 70 - 150$ Myr.

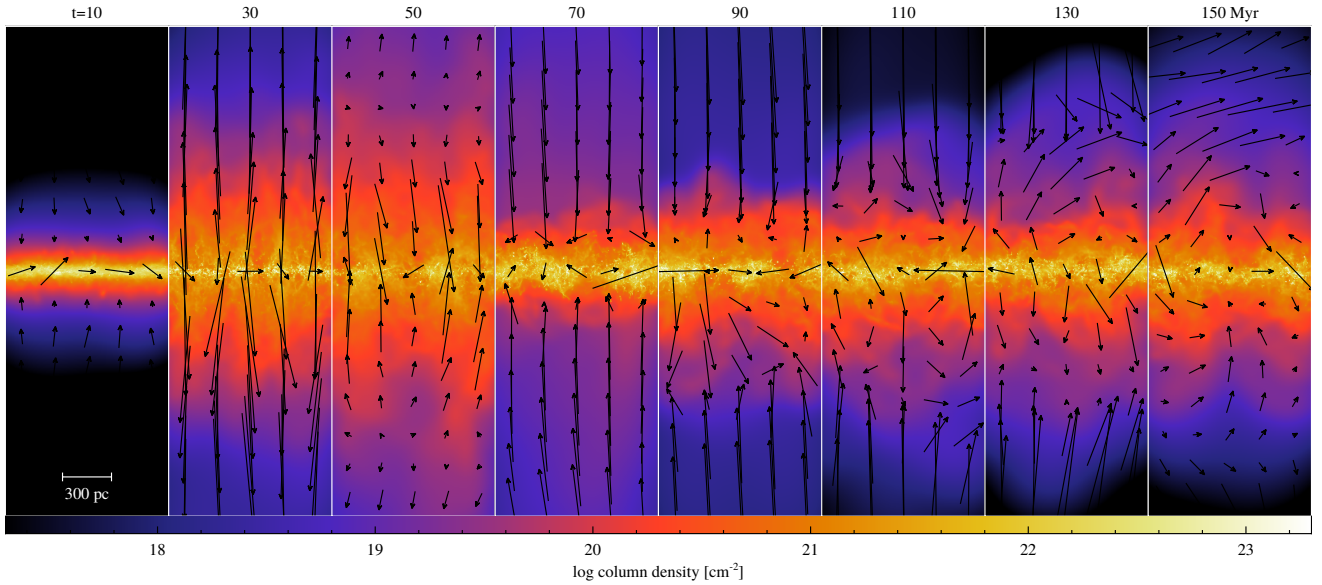


Figure 2. Same as Fig. 1 but for the PH simulation.

magnitude is $|\mathbf{F}_r| = \tilde{c}E_r$, where E_r is the photon energy density and \tilde{c} is the reduced speed of light, which in our simulations is set to 10^3 km s $^{-1}$. This overcomes the issues mentioned in Hopkins & Grudic (2018) by ensuring that the full radiation pressure force is accounted for even if the cell optical depth is larger than one. However, this leads to anisotropic pressure forces around a star particle, but this is mitigated by the fact that we form a large number of stars during the simulation and each random orientation adds up to create an isotropic pressure force.

We perform four different simulations; SN: only the SNe feedback is active; PH: SN + photoheating from UV sources is active; RP: PH + radiation pressure from just single scattering UV radiation is active and finally IR: RP + effect of multi scattered IR radiation. Each of these simulations are run for $t = 150$ Myr. In this paper we have decided to focus only on the effect of radiation fields and hence our simulations neglect the effects of other important ingredients such as the magnetic field, winds from massive stars, and cosmic rays.

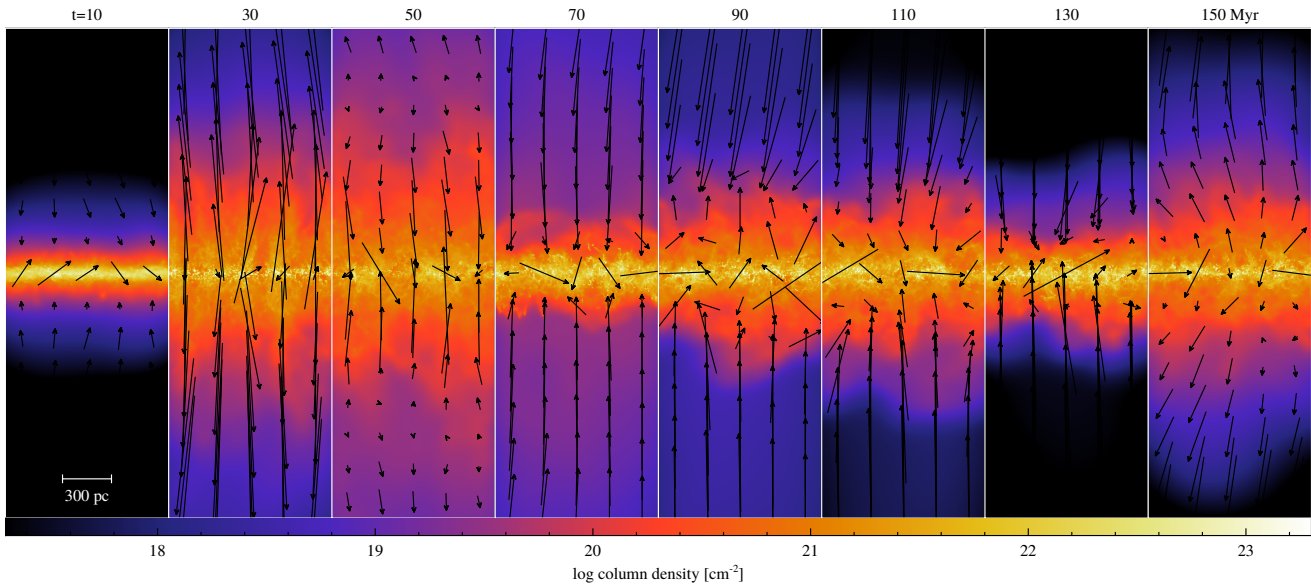


Figure 3. Same as Fig. 1 but for the RP simulation.

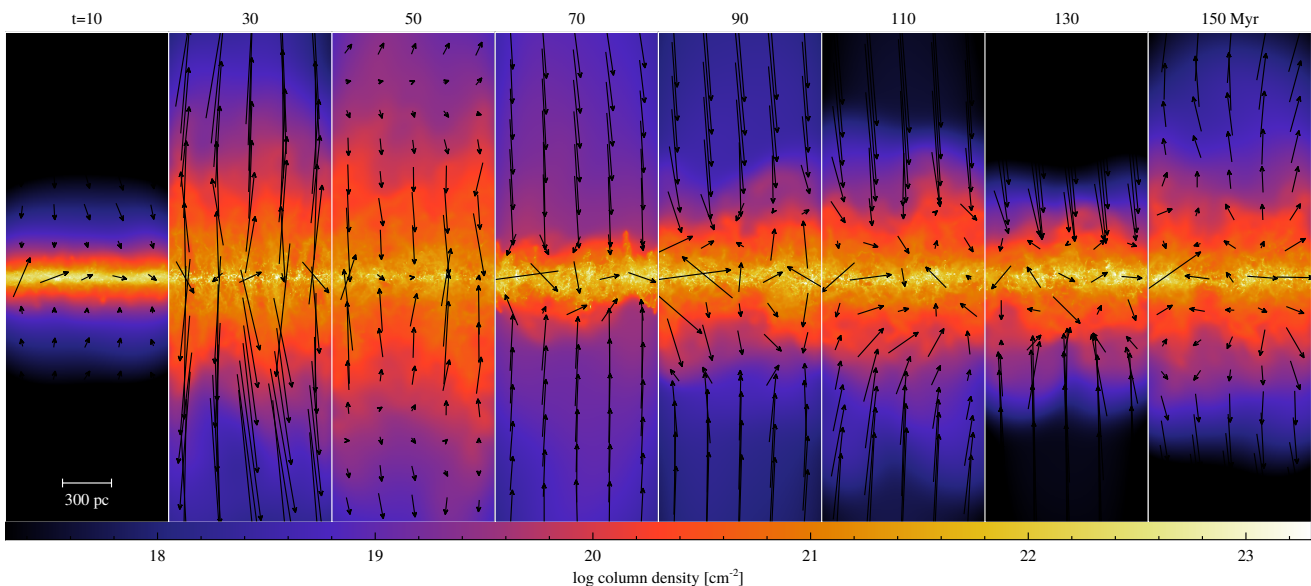


Figure 4. Same as Fig. 1 but for the IR simulation.

3 RESULTS

We begin by looking at the morphological evolution of the disc in our simulations. Fig. 1 shows the $x-z$ (1×3 kpc) map of the column density integrated along the y -axis in the SN simulation at $t = 10$ (first column), 30 (second column), 50 (third column), 70 (fourth column), 90 (fifth column), 110 (sixth column), 130 (seventh column) and 150 (eighth column) Myr. The black arrows indicate the direction of the velocity field with the length of the arrows representing its magnitude. During the initial 10 Myr, the disc cools and contracts before the first stars form and explode as SNe. This causes a small scale inflow which reduces the scale height of the disc and induces a starburst. As the stars begin injecting feedback

energy into the ISM, it starts to drive an outflow. This outflow period lasts up to ~ 50 Myr, during which time the disc scale height increases. The outflow reaches up to ~ 4 kpc, stalls and begins to fall back to the disc. This inflow period lasts up to 75 Myr. The disc then settles down and forms stars at a constant rate which creates a small scale ($\lesssim 1$ kpc) fountain flow. The outflow velocities generated during the star-burst phase of evolution is generally higher compared to the fountain flow phase.

The morphological evolution of the disc in the PH (Fig. 2), RP (Fig. 3) and IR (Fig. 4) simulations is qualitatively quite similar, with a prominent starburst driven outflow phase followed by an inflow phase and a small-scale fountain flow phase. However, there are some interesting differences between the SN run and the

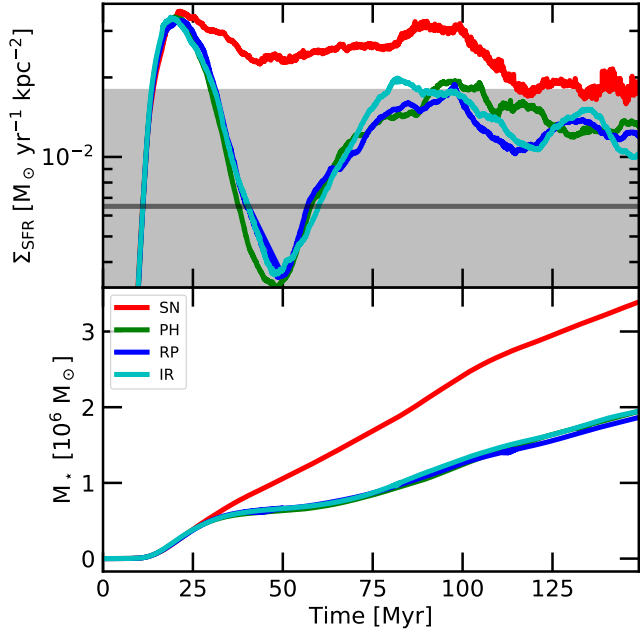


Figure 5. The star formation rate surface density (top panel) and the total amount of stellar mass formed (bottom panel) as a function of time (in Myr) in the SN (red curves), PH (green curves), RP (blue curves) and IR (cyan curves) simulations. The solid grey line depicts the expected star formation rate from the Kennicutt-Schmidt relation (Kennicutt & Evans 2012) and the grey shaded region is the factor of three observational error in the observed relation. After the initial starburst, the simulations with ESF show a steep drop in the SFR, which slowly bounces back and regulates to a value by a factor of ~ 2 lower than in SN run. The total amount of stars formed is also reduced by a factor of ~ 1.5 in the runs with ESF. The negligible difference between the PH, RP and IR runs shows the inability of radiation pressure (both single and multi-scattering) to regulate star formation in low surface density galaxies.

runs with radiation fields (or runs with early stellar feedback or ESF runs). Throughout the simulation, the central high density disc remains relatively unperturbed in the SN run while the ESF runs manage to make the ISM more clustered creating low density holes and filamentary channels through which material can be ejected without hindrance. This allows the ESF runs to drive gas flows to larger heights above the disc. This difference is clearly visible during the initial starburst period ($t = 30 - 50$ Myr). They are also able to entrain more high density material in the outflow in both the starburst and fountain flow period of the evolution. These column density maps shows that including radiation fields makes stellar feedback qualitatively more effective. Most of the difference is seen between the SN and PH runs and there is very little difference between the PH, RP and IR runs, implying that photoheating is the primary mechanism through which radiation fields interact with the ISM and radiation pressure has minimal effect in regulating star formation and driving outflows in our model.

We begin a more quantitative comparison by plotting the star formation rate surface density (top panel) and the total stellar mass formed (bottom panel) with time in the SN (red curves), PH (green curves), RP (blue curves) and IR (cyan curves) simulations (Fig. 5). The solid grey line depicts the expected star formation rate from the Kennicutt-Schmidt relation (Kennicutt 1998; Kennicutt & Evans 2012) and the grey shaded region is the factor of three observational error in the observed relation. The amplitude of the initial starburst

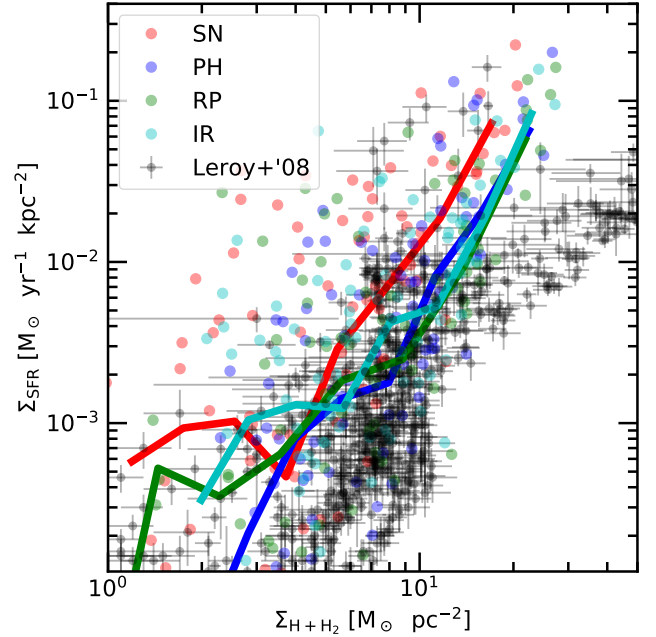


Figure 6. The star formation rate surface density as a function of the hydrogen ($H+H_2$) surface density in the SN (red), PH (green), RP (blue) and IR (cyan) simulations. The data is taken at the simulation time of $t = 150$ Myr. The individual points are obtained by dividing the disc into patches of size 100×100 pc and calculating both quantities for each patch. The solid lines denote the median for each simulation. For comparison, the observational estimates from Leroy et al. (2008) are plotted with black circles. The runs with ESF tend to bring the values close to the observed estimates.

is similar in all simulations. This is expected, because the stars have not had the time to feed energy back into the ISM. After about 20 Myr, the SFR curves start to deviate. The SN run continues to form stars at a very high rate ($\sim 0.02 - 0.03 M_\odot \text{ yr}^{-1} \text{ kpc}^{-2}$), while all three runs with radiation fields show a precipitous drop in the SFR's, with the minimum as low as $\sim 0.003 M_\odot \text{ yr}^{-1} \text{ kpc}^{-2}$. By about 75 Myr the SFR's bounce back and saturate to a value that is about $1.5 - 2$ lower than the SFRs obtained from the SN simulation. The SFR in the SN run always remains above the observed value throughout the simulation, matching the SFR estimates from the simulation including only SNe feedback presented in Peters et al. (2017). We note that the drop off in the SFR surface density at about ~ 100 Myr is due to the significant decrease in the gas surface density by $\sim 30\%$ due to the conversion of gas into stars. The ESF runs on the other hand manage to contain the SF within observational limits, even with higher gas surface density at late times, though it must be noted that it is at the upper end of the observed error margin. The total stellar mass formed in the ESF runs are also about factor of two lower than the SN simulation. There is very little difference between the PH, RP and IR runs, implying that radiation pressure, both UV and IR, is unimportant in these low density environments. Photoheating, therefore, emerges as the most important early stellar feedback mechanism, which is in agreement with previous works (Stinson et al. 2013; Kannan et al. 2014b; Sales et al. 2014; Rosdahl et al. 2015).

Fig. 6 shows the star formation rate surface density as a function of the gas ($H + H_2$) surface density at $t = 150$ Myr, for the SN (red curves), PH (green curves), RP (blue curves) and IR (cyan curves) simulations. The observational data points (black circles)

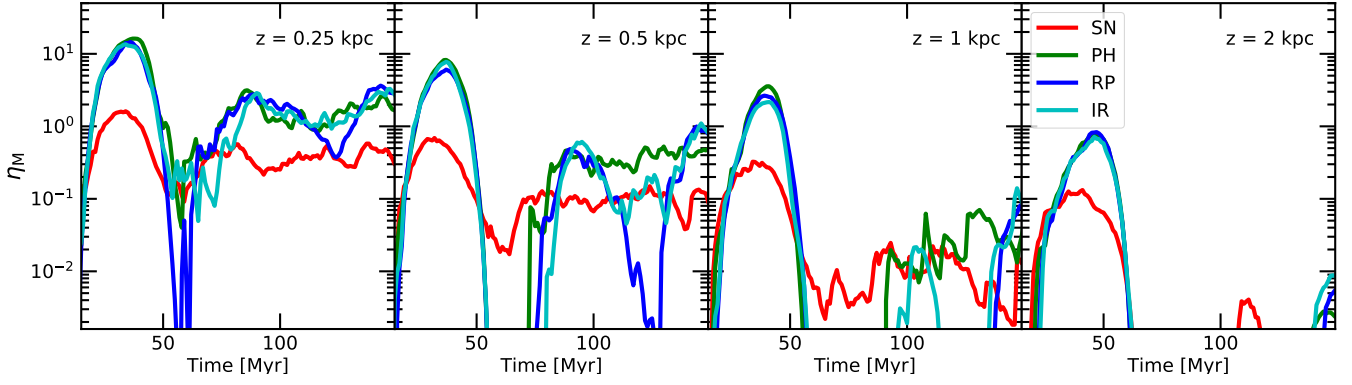


Figure 7. The mass loading factor (defined as $\eta_M = \dot{M}_{\text{out}}/\dot{M}_*$) as a function of time at $z = 0.25$ (first panel), $z = 0.5$ (second panel), $z = 1.0$ (third panel) and $z = 2.0$ (fourth panel) kpc above the disc for the SN (red curves), PH (green curves), RP (blue curves) and IR (cyan curves) simulations. η_M generally decreases with z for all the runs and the runs with ESF generally have higher η_M 's at all times.

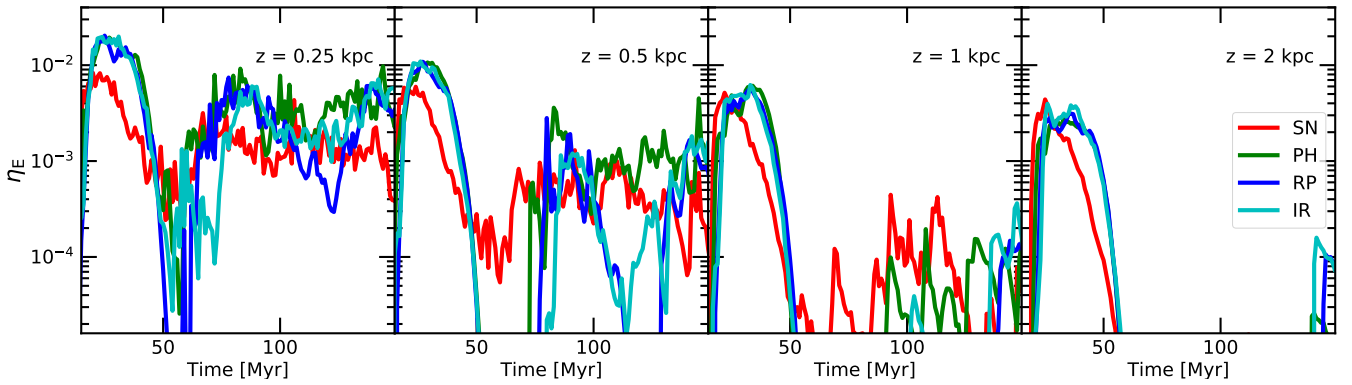


Figure 8. The energy loading factor (defined as $\eta_E = \dot{E}_{\text{out}}/\dot{E}_{\text{SNe}}$) as a function of time at $z = 0.25$ (first panel), $z = 0.5$ (second panel), $z = 1.0$ (third panel) and $z = 2.0$ (fourth panel) kpc above the disc for the SN (red curves), PH (green curves), RP (blue curves) and IR (cyan curves) simulations.

are obtained from observations of 23 nearby galaxies as outlined in Leroy et al. (2008). The individual data points from our simulations are obtained from dividing the disk into 100×100 pc chunks and calculating both the quantities for each chunk. This allows us to study the KS relation in a wide variety of environments. The solid lines indicate the median values, which generally lie within the cloud of observed data points. Including radiation fields brings the simulated KS relation closer to the observed values. We do however, somewhat overshoot the relation possibly hinting at missing important physical processes like stellar winds, cosmic rays or the effect of binary stars leaving their birth clouds and exploding in low density environments.

We now turn our attention to the key quantities that describe a SNe driven wind, the mass (η_M) and energy (η_E) loading factors. The mass loading factor at a height z from the plane of the disc is defined as the ratio between the outgoing mass flux and the star formation rate:

$$\eta_M|_z = \frac{\dot{M}_{\text{out}}(z)}{\dot{M}_*}. \quad (7)$$

Similarly, the energy loading factor at z is defined as the ratio of the total energy flux carried away by the wind to the energy injection rate by SNe:

$$\eta_E|_z = \frac{\dot{E}_{\text{kin,out}} + \dot{E}_{\text{therm,out}}}{E_{\text{SN}}\dot{M}_*}, \quad (8)$$

where $E_{\text{SN}} = 10^{51}$ erg/ $100 M_\odot$. \dot{M}_{out} and \dot{E}_{out} are calculated only for gas that has a z velocity vector pointing away from the disc midplane (i.e., we do include any inflowing gas in our analysis of mass and energy loading factors). It is important to quantify these quantities as sub-grid feedback models generally prescribe the mass, energy and metal loading factors and tune them in order to reproduce the observed galaxy properties (Vogelsberger et al. 2013).

Fig. 7 shows the mass loading factor at 0.25 kpc (first panel), 0.5 kpc (second panel), 1 kpc (third panel) and 2 kpc (fourth panel) above the disc for the SN (red curves), PH (green curves), RP (blue curves) and IR (cyan curves) simulations. The behaviour of η_M is qualitatively similar in all the runs, with its value peaking during the initial starburst-driven outflow phase, followed by a decrease during the inflow phase and a rebound, at least close to the disc, during the fountain flow period. During the initial starburst period, the SN simulation drives outflows with a mass loading of ~ 2 at $z = 0.25$ kpc which gradually drops to a value of about ~ 0.1 at $z = 2$ kpc. This weak outflow leaves the disc relatively unaltered, which allows the SF to continue at a relatively high rate even during the post-starburst period. The slight decrease in the SFR leads to a nominal decrease in η_M at low z ($\lesssim 1$ kpc). The mass loading at high z 's, however, shows a large drop off because the lower SFR's combined with a puffier disc makes SNe feedback

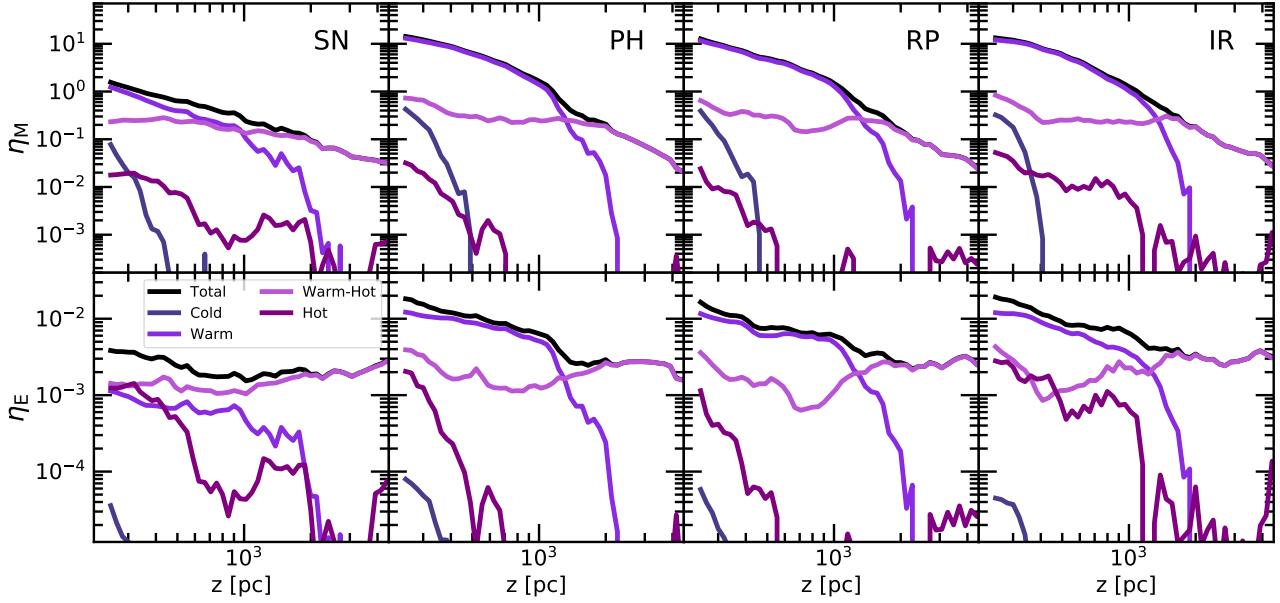


Figure 9. The mass (top panels) and energy loading (bottom panels) factors as a function of height from the disc (z) for cold ($T \leq 300$ K), warm ($300 < T \leq 8000$ K), warm-hot ($8000 < T \leq 3 \times 10^5$ K) and hot gas ($T > 3 \times 10^5$ K) during the outflow phase of the simulation, $t = 30$ Myr. The first column shows the values for the SN simulation, second column; PH, third column; RP and fourth column; IR. Most of the mass and energy of the outflow is in the warm and warm-hot phases, with the cold and hot gas being subdominant. The increase in mass and energy loading factors in the runs with ESF is primarily driven by the increase in outflow of the warm phase.

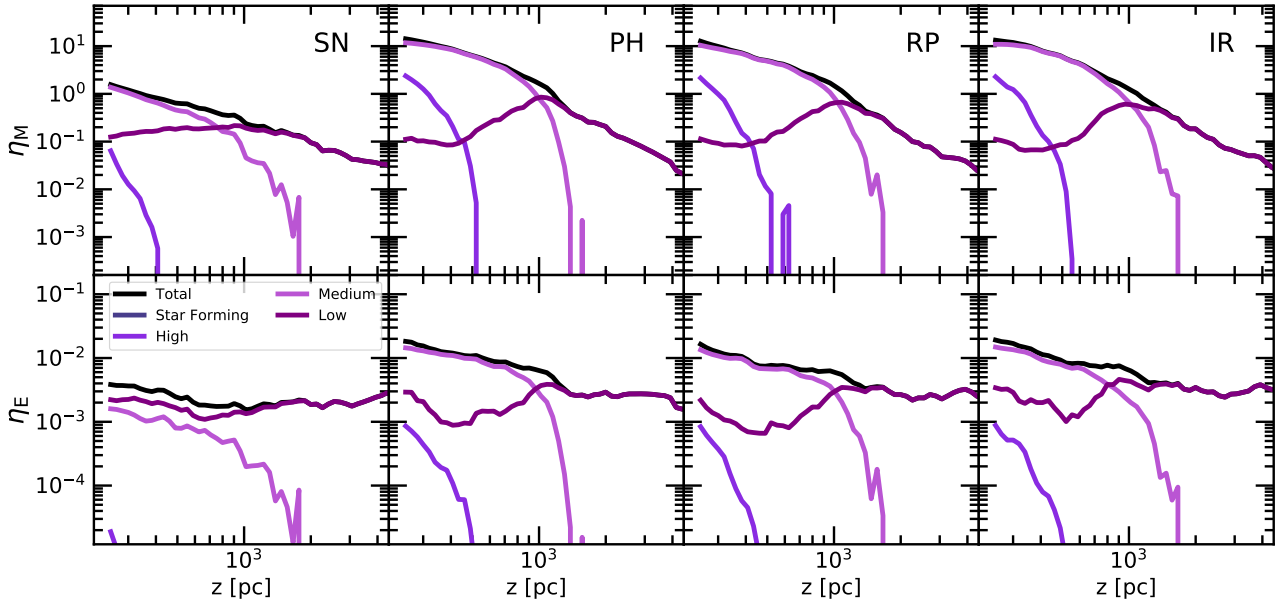


Figure 10. The mass (top panels) and energy loading (bottom panels) factors as a function of height from the disc (z) for star-forming ($n \geq 10^2 \text{ cm}^{-3}$), high ($1 \leq n < 10^2 \text{ cm}^{-3}$), medium ($10^{-2} \leq n < 1 \text{ cm}^{-3}$) and low ($n < 10^{-2} \text{ cm}^{-3}$) density gas during the outflow flow phase of the simulation, $t = 30$ Myr. The first column shows the values for the SN simulation, second column; PH, third column; RP and fourth column; IR.

less efficient. Under these conditions feedback is able to drive only a small-scale fountain flow up to a height of $z \sim 1$ kpc.

The quantitative picture in the ESF runs is quite different. The peak mass loading is much higher with a value of ~ 20 close to the disc and ~ 1 at $z = 2$ kpc. This blows out most of the gas from the disc causing the large drop off in the SF (see Fig. 5) during the post starburst phase of the simulations. During this phase of evolution ($t = 25 - 50$ Myr), η_M in the ESF runs drops precipitously. This is

caused by the large drop off in the star formation by almost a order of magnitude which reduces the pressure behind the outflow, making it stall and fall back onto the disc. Once the disk settles down η_M rebounds to values of about $2 - 3$ close to the disc, while there is very little gas at $z \gtrsim 1$ kpc. We note that this value is higher than that obtained in the SN simulation by a factor of $5 - 10$. It is quite clear that a true large scale wind is only launched during the initial starburst phase, while only a small scale fountain flow operates

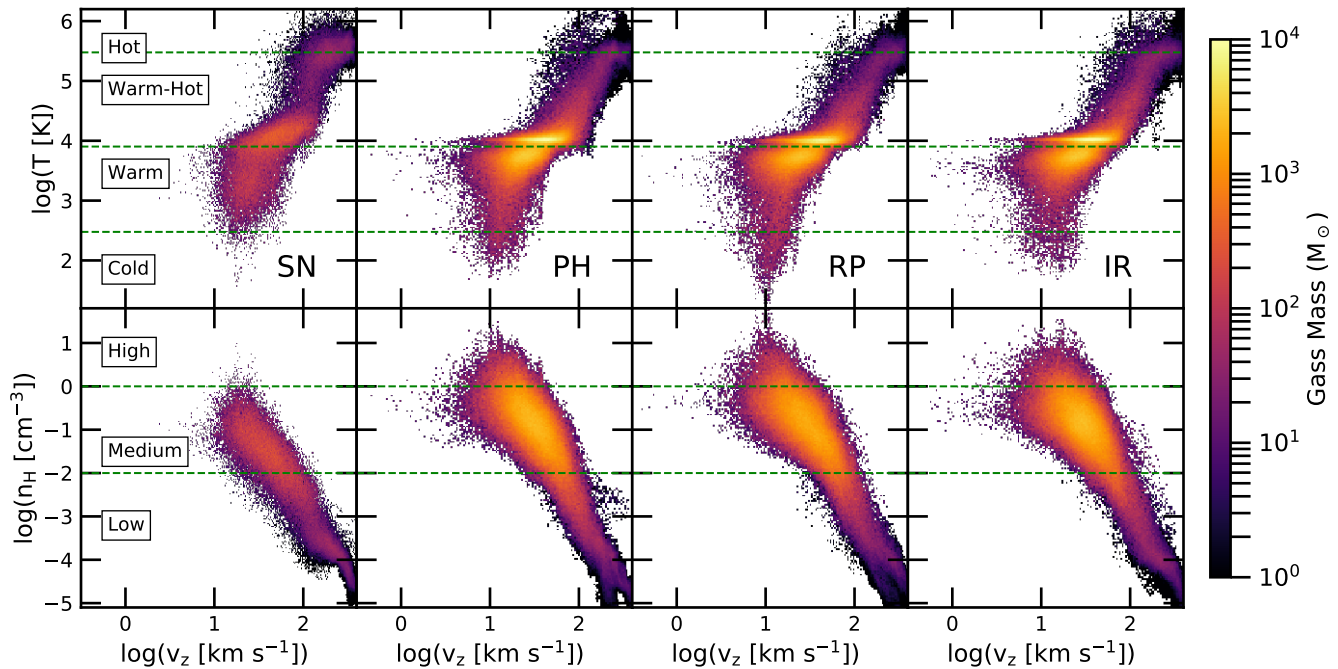


Figure 11. The temperature (top panels) and density (bottom panels) histograms of the outflowing gas as a function of the outflow velocity at $t = 30$ Myr for the SN (first column), PH (second column), RP (third column) and IR (fourth column) simulations.

after $t > 75$ Myr in all the runs. The initial starburst in our simulations is caused by the gas radiatively cooling, losing its pressure support and settling down in the external gravitational potential into a thin disk. This is compounded by the fact that the main channel of feedback in our simulations, SNe, are only active 5 Myr after the first stars form. Therefore, self-regulation during this initial period is not possible. Changes in initial conditions and parameters such as the time period between star formation and SNe feedback will change the duration and strength of the starburst. While, the reasons for a starburst in the simulations are largely dictated by the way the initial conditions of our simulations are constructed, the difference between the evolution of SN and ESF simulations is quite dramatic and deserves further examination. Furthermore, an analogy can be made to the systems that have undergone a starburst during a merger making the scenario of a post merger starburst induced quenching in galaxies more probable.

Fig. 8 shows the energy loading factor at 0.25 kpc (first panel), 0.5 kpc (second panel), 1 kpc (third panel) and 2 kpc (fourth panel) above the disc for the SN (red curves), PH (green curves), RP (green curves) and IR (cyan curves) simulations. The evolution of η_E is qualitatively quite similar to the evolution in η_M , with the peak η_E occurring at about the same time as the occurrence of peak η_M at $t \sim 30$ Myr, followed by a precipitous drop in the post starburst period for the ESF runs and the existence of a small-scale fountain flow with low energy loading after $t \gtrsim 75$ Myr. Peak η_E in the ESF runs ranges from ~ 0.02 at $z = 0.25$ kpc to 3×10^{-3} at $z = 2$ kpc. Interestingly, the peak energy loading in the SN simulation remains constant at about 3×10^{-3} across different heights from the disc. At late times value of η_E in the ESF runs is about 2 – 3 times larger than in SN run close to the disc ($z \lesssim 1$ kpc). It is difficult to make any claims about η_E above this height because of the absence of outflowing material.

A more comprehensive picture of the outflow behaviour can

be obtained by decomposing (Fig. 9) the mass (top panels) and energy (bottom panels) loading into the different temperature bins at the peak of the outflow ($t = 30$ Myr) as a function of height from the disc. The dark blue curves indicate η_M and η_E for cold ($T < 300$ K) gas, violet curves for the warm ($300 \text{ K} \leq T < 8000$ K) gas, orchid curves for the warm-hot ($8000 \text{ K} \leq T < 3 \times 10^5$ K) gas and purple curves, the hot ($T \geq 3 \times 10^5$ K) gas. Close to the disc, the SN run has a mass loading of about ~ 2 and decreases to 0.02 by $z \sim 4$ kpc, the energy loading remains constant at about 3×10^{-3} . The ESF runs on the other hand, have η_M of ~ 10 close to the disc which, reduces to ~ 0.02 by about ~ 4 kpc, while η_E ranges from 0.02 to $\sim 2 \times 10^{-3}$. Cold gas is never entrained in the outflow irrespective of the simulation we consider. The hot phase in the SN run has slightly higher mass and energy loading compared to the ESF runs. However, both these phases are subdominant to the warm and warm-hot gas phases. The warm-hot gas has roughly a constant mass ($\eta_M \sim 0.1$) and energy ($\eta_E \sim 2 \times 10^{-3}$) loading up to $z = 4$ kpc, implying the existence of a true large-scale wind (Kim & Ostriker 2017). Including radiation fields only slightly increases η_M and η_E of this phase but drastically boosts it for the warm gas, especially at low z (< 2 kpc). This effect is so large that the higher mass and energy loading in the ESF runs at low z is almost entirely driven by the increase in the warm phase of the outflow. This implies that the runs with radiation fields are able to entrain more warm material in the outflow and eject it to distances of about 2 kpc from the disc. Therefore, the ESF runs launch a more pronounced small scale, warm fountain flow in addition to the large scale warm-hot wind during the starburst phase. This also explains the almost constant total energy loading in the SN run, contrasted to the declining energy loading in the ESF runs.

A similar analysis can be performed by decomposing the outflow into star forming ($n \geq 10^2 \text{ cm}^{-3}$; dark blue curves), high

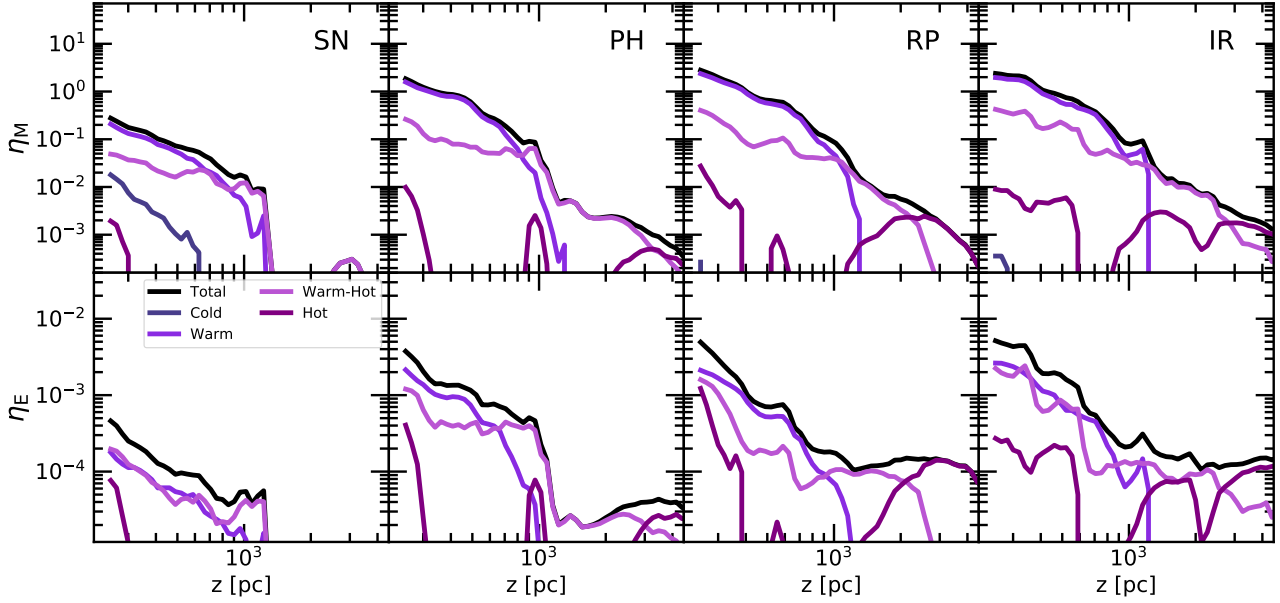


Figure 12. The mass (top panels) and energy loading (bottom panels) factors as a function of height from the disc (z) for cold ($T \leq 300$ K), warm ($300 < T \leq 8000$ K), warm-hot ($8000 < T \leq 3 \times 10^5$ K) and hot gas ($T > 3 \times 10^5$ K) during the fountain flow phase of the simulation, $t = 150$ Myr. The first column shows the values for the SN simulation, second column; PH, third column; RP and fourth column; IR. η_M and η_E are lower than during the outflow phase of the simulation, but the trends are quite similar.

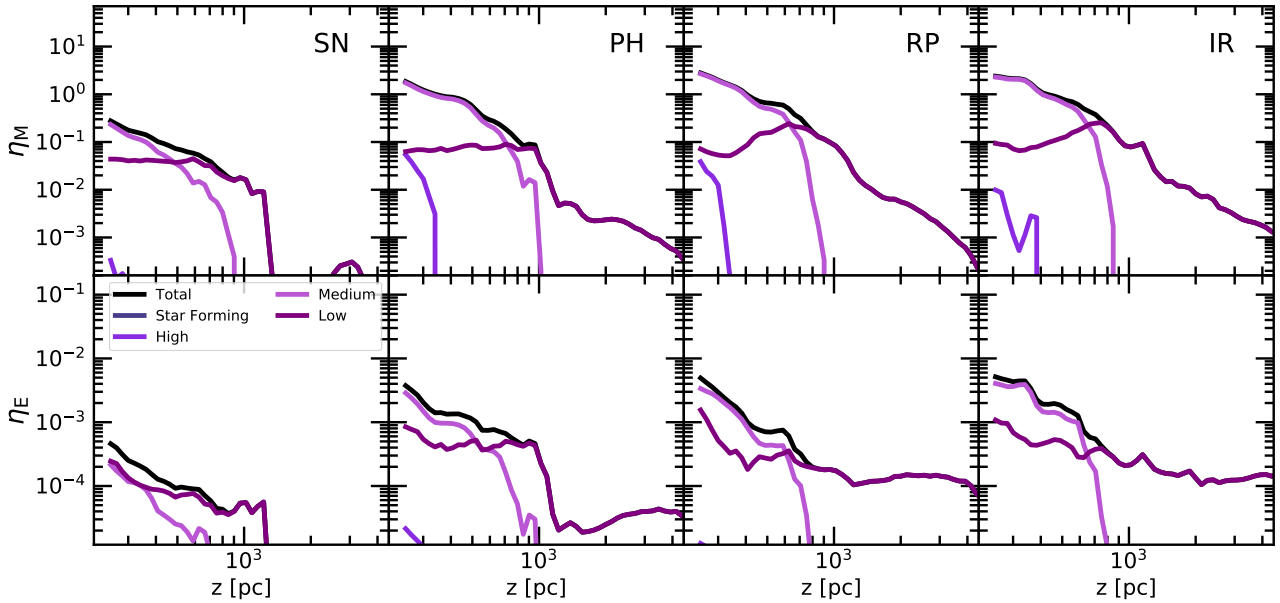


Figure 13. The mass (top panels) and energy loading (bottom panels) factors as a function of height from the disc (z) for star forming ($n \geq 10^2 \text{ cm}^{-3}$), high ($1 \leq n < 10^2 \text{ cm}^{-3}$), medium ($10^{-2} \leq n < 1 \text{ cm}^{-3}$) and low ($n < 10^{-2} \text{ cm}^{-3}$) density gas during the fountain flow phase of the simulation, $t = 150$ Myr. The first column shows the values for the SN simulation, second column; PH, third column; RP and fourth column IR.

($1 \leq n < 10^2 \text{ cm}^{-3}$; violet curves), medium ($10^{-2} \leq n < 1 \text{ cm}^{-3}$; orchid curves) and low ($n < 10^{-2} \text{ cm}^{-3}$; purple curves) density gas (Fig. 10). The density structure of the outflow in many ways mirrors its temperature structure. There is no entrainment of the star forming gas in any of the runs. Some amount of high density gas is launched upto heights of $z \lesssim 0.5 \text{ kpc}$ and the η_M and η_E for this phase in the ESF runs is about 10 times larger than in the SN run. The outflow is mostly dominated by the medium and low density material. The medium density gas forms a fountain flow

that reaches heights of $z \lesssim 2 \text{ kpc}$ while the low density material forms a true large scale wind. The mass and energy loading of the low density wind is quite similar in the SN and ESF runs, but the medium density fountain flow is about 10 times more mass and energy loaded in the ESF runs compared to the SN run. Therefore a picture emerges of a starburst driven outflow that can be decomposed into two distinct phases, a small-scale ($\sim 2 \text{ kpc}$) fountain flow mainly composed of warm ($300 \leq T < 8000 \text{ K}$), medium density ($0.01 \leq n < 1 \text{ cm}^{-3}$) gas and a large scale wind ($\gtrsim 4 \text{ kpc}$)

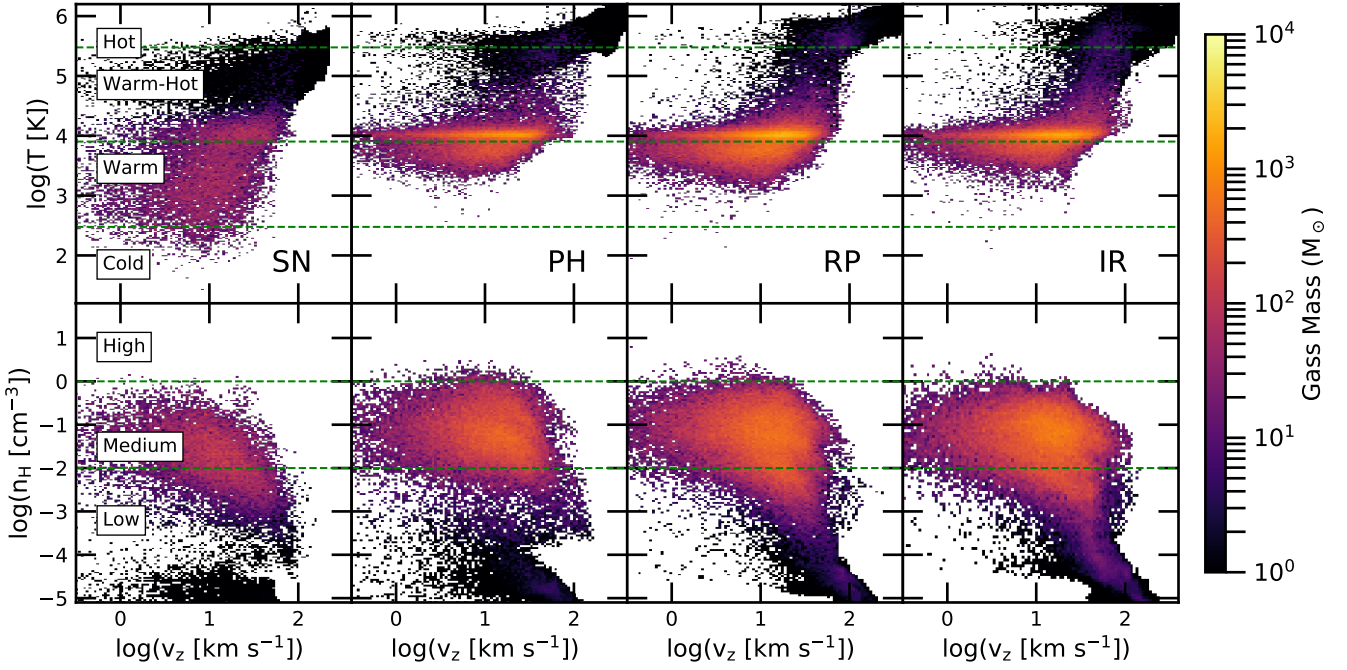


Figure 14. The temperature (top panels) and density (bottom panels) histograms of the outflowing gas as a function of the outflow velocity at $t = 150$ Myr for the SN (first column), PH (second column), RP (third column) and IR (fourth column) simulations.

that is composed of warm-hot ($8000 \leq T < 3 \times 10^5$ K), low density ($n < 10^{-2} \text{ cm}^{-3}$) material. We conclude that radiation fields coupled with SNe have the effect of launching colder, denser and higher mass loaded outflows compared to feedback models that do not consider this process.

In order to better understand the multiphase, multi-component nature of the outflow we plot (Fig. 11) the temperature-outflow velocity (top panels) and density-outflow velocity (bottom panels) histograms in the SN (first column), PH (second column), RP (third column) and IR (fourth column) simulations. This plot considers all the gas that is moving outward from the disc and at a height $z > 250$ pc as part of the outflow. The green horizontal lines divide the outflow into star forming, high, medium and low density gas and similarly into cold, warm, warm-hot and hot gas. There is a very clear trend towards higher velocities for higher temperature and lower density gas. There are some very interesting differences between the SN and ESF runs. The amount of gas mass in the outflow is much larger in the runs with radiation fields. ESF runs are also able to entrain more cold and high density material. More importantly the warm-medium density gas phase is more mass loaded in the ESF runs. The velocity of this phase is however less than $\sim 100 \text{ km s}^{-1}$, meaning that it cannot get very far from the disc, thereby generating a small scale fountain flow. The material with velocities larger than 100 km s^{-1} go on to generate the large scale wind which is both low density and hot. This explains the mass and energy loading behaviour of the outflows in our simulations. We note that the outflows described here are unlikely to reach wind velocities large enough to be unbound from the galaxy, because the Milky Way escape velocity at the solar circle probably exceeds 500 km s^{-1} (Smith et al. 2007).

A similar analysis can be performed in the fountain flow phase of the simulation ($t > 75$ Myr). Fig. 12 decomposes the mass (top panels) and energy (bottom panels) loading into the different

temperature bins during the fountain flow phase of the simulation at $t = 150$ Myr as a function of height from the disc. The mass and energy loading factors are lower than in the starburst phase as expected. Moreover, they decline quite quickly as the height above the disc increases, which is a clear sign of a fountain flow. Close to the disc, the SN run has a mass loading of about ~ 0.2 and decreases to $< 10^{-3}$ by $z \sim 1 \text{ kpc}$, the energy loading goes from 6×10^{-4} to $\lesssim 10^{-4}$ in the same range. The ESF runs on the other hand, have η_M of about ~ 2 close to the disc and reduces to $\sim 10^{-3}$ at about $\sim 4 \text{ kpc}$ and η_E ranges from 3×10^{-3} to $\sim 5 \times 10^{-4}$. In the SN run, none of the temperature phases reach beyond $z \gtrsim 1 \text{ kpc}$. This is not the case in the runs with radiation fields, where, the warm-hot material reaches heights of $\sim 3 \text{ kpc}$ and above this height the hot phase starts to dominate the outflow. The warm phase dominates both the mass and energy loading of the outflow within about $z = 1 \text{ kpc}$ in the ESF runs, but remains sub-dominant in the SN run.

Fig. 13 decomposes the outflow into the star forming, high, medium and low density gas (Fig. 10) at $t = 150$ Myr. Similar to the starburst phase, the density structure of the fountain flow in many ways mirrors its temperature structure. There is no entrainment of the star forming gas in any of the runs. The SN run manages to entrain very little high density material but the ESF runs can entrain and launch this material up to $z \leq 0.3 \text{ kpc}$. Most of the mass and energy loading in the ESF runs at low z ($\lesssim 1 \text{ kpc}$) is dominated by the medium density gas, whereas, in the SN run, the low density gas dominates at all heights except in the very center. There is no appreciable gas above $z > 1 \text{ kpc}$ in the SN run, but there is some in the ESF runs, with most of the gas at this height composed of low density-hot material. The additional entrainment of the medium density gas increases the mass and energy loading in the ESF runs by a factor of $\sim 5 - 10$.

Fig. 14 shows the the temperature-outflow velocity (top pan-

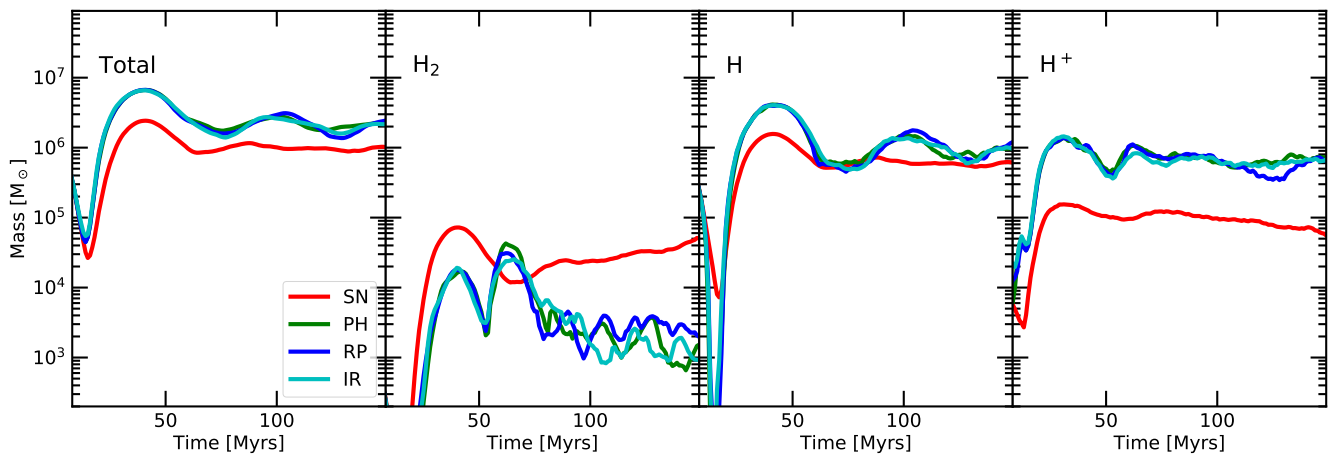


Figure 15. The chemical composition for the ejected outflow as a function of time in the SN (red curves), PH (green curves), RP (blue curves) and IR (cyan curves) simulations. The ejected material is defined as any material with $z > 250$ pc. The first column shows the total amount of ejected gas, the second column – mass in molecular hydrogen (H_2), third column – neutral hydrogen and the fourth column – mass of ionized hydrogen.

els) and density-outflow velocity (bottom panels) histograms in the SN (first column), PH (second column), RP (third column) and IR (fourth column) simulations at $t = 150$ Myr. All gas that is moving outward from the disc and at a height $z > 250$ pc is considered a part of the outflow. The green horizontal lines divide the outflow into star forming, high, medium and low density gas and similarly into cold, warm, warm-hot and hot gas. The amount of mass in the outflow is much lower than during the starburst phase. The cold high density phase no longer exists. There is very little gas with velocities $v_z \gtrsim 100 \text{ km s}^{-1}$, explaining the lack of a large scale wind. In the runs with radiation fields, most of the gas is photoionized and has a temperature of $\sim 10^4$ K. The medium density - warm-hot phase is more mass loaded in the ESF runs compared to the SN run. It is therefore, quite clear that even in the low star formation mode of evolution, radiation fields make stellar feedback more efficient. They do not generate large scale winds, but are able to launch low temperature, higher density outflows that are higher mass and energy loaded. These outflows reach heights of about 1 – 2 kpc from the disc, forming a robust fountain flow. In contrast just SNe feedback creates a weak fountain flow that consists of mainly very low density hot gas. This is despite the fact that the ESF runs have about two times lower SFR than the SN run. Importantly, η_M and η_E are about a factor of $\sim 5 - 10$ larger in the presence of radiation fields and this increase is mainly driven by the entrainment of warm, dense material in the outflowing gas. This quantitative result holds true in both the starburst and fountain flow phases of the simulation therefore implying that this is a very robust prediction.

To assess the impact of radiation fields on the chemical composition of the outflowing gas, we plot in Fig. 15 the masses of the ejected material in terms of different hydrogen species as a function of time in the SN (red curves), PH (green curves), RP (blue curves) and IR (cyan curves) simulations. The ejected material is defined as any gas present above $z = 250$ pc at any given point in time. The first column shows the total amount of ejected gas, the second column – mass in molecular hydrogen H_2 , third column – neutral hydrogen and the fourth column – mass of ionized hydrogen. As expected, the total amount of gas ejected from the disc is higher in the ESF runs, by about a factor of ~ 5 during the starburst period and about ~ 2 at the later stages ($t \gtrsim 75$ Myr). The

fraction of gas in the molecular state is quite low ($< 5\%$) in all the runs. This is expected because the density of gas at these heights is quite low $< 1 \text{ cm}^{-3}$. However, the lack of any radiation fields in the SN run allows for a comparatively large molecular fraction in the outflow. This picture will definitely change if the metagalactic background is included. The larger amount of cold, dense gas in the ESF outflows, does allow for self-shielding of the hydrogen molecule giving rise to a larger fraction of neutral hydrogen gas in the outflow. Finally, we note that the illumination of the ejected gas by the radiation fields from the disc increases the abundance of ionized hydrogen by almost a factor of ~ 10 . Therefore, we conclude that the ESF runs give rise to an ejecta that is half-ionized and half neutral, whereas the ejecta in the SN run is mainly neutral due to the absence of radiation fields.

4 DISCUSSION

On the whole the runs with radiation fields increase the mass and energy loading factor by about a factor of 5 – 10, close to the disc ($z < 1$ kpc), throughout the entirety of the simulation time. They are still lower by about 2 – 3 when compared to random driving (SNe explosions occur at random positions) tall box simulations presented in Girichidis et al. (2016). The motivation of these simulations was to get the structure of the ISM right, meaning that the mass and energy loading factors were not tuned to match observations. On the other hand our values are closer to the those predicted by global galaxy simulations with more realistic geometries (Muratov et al. 2015; Fielding et al. 2017) and with analytic estimates of the values required to explain the observed galaxy stellar mass function and the metal enrichment of the intergalactic medium (Somerville & Davé 2015). However, our tallbox geometry implies that the wind mass and energy loading factors are not well-defined because they decline significantly with increasing box height (See Section 5 for more details). Despite this caveat, it is quite clear that early stellar feedback does indeed play an important role in regulating star formation and launching outflows. The consistently lower SFRs in the ESF runs indicate that radiation fields make feedback more efficient. There are two ways in which the radiation fields can reduce star formation. They can heat up the disc

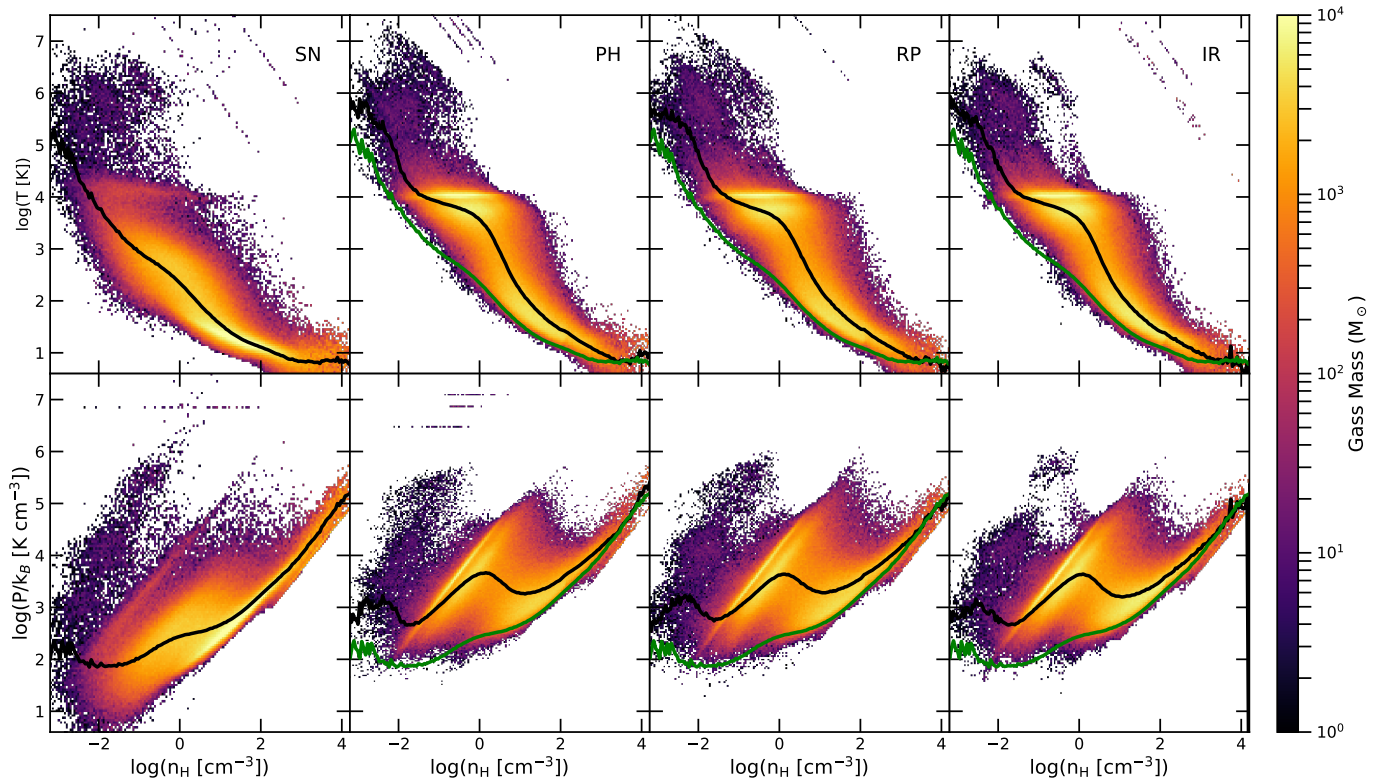


Figure 16. The temperature-density (top panels) and pressure-density (bottom panels) phase space diagram of the disc ($z < 250$ pc) at $t = 150$ Myr for the SN (first column), PH (second column), RP (third column) and IR (fourth column) simulations. In general for a given density the gas temperature and therefore pressure is higher for the runs with ESF. The black lines denote the median of the distribution and the solid green lines in the ESF runs denote the median obtained from the SN simulation.

through photoheating, which increases the temperature in the disc, puffing it up and reducing the star formation. Secondly, photoheating and radiation pressure can evacuate gas from the neighbourhood of newly formed stars allowing them to explode in relatively low density environments. This increases the momentum output of SNe explosions by reducing the cooling losses (Martizzi et al. 2015). There is evidence for both these effects in our simulations.

Fig. 16 shows the temperature-density (top panels) and pressure-density (bottom panels) phase space diagram of the gas in the disc (defined as $z < 250$ pc) at $t = 150$ Myr in the SN (first column), PH (second column), RP (third column) and IR (fourth column) simulations. The black solid lines show the median of the distribution. For comparison, the median obtained from the SN simulation is plotted in the ESF runs in solid green lines. Only the ESF runs show a true two-temperature multiphase medium in pressure equilibrium. For a given density the temperature and therefore the pressure of the gas is higher in the runs with radiation fields. This higher pressure provides additional support against gravitational collapse, puffing up the disc and reducing the star formation rate. This effect can be quantified by looking at the vertical structure of the disc. A simple estimate is obtained by calculating the height which encloses 60% of the total mass of the disc ($H_{60\%}$) and contrasting it with $H_{90\%}$, the height which encloses 90% of the total mass. $H_{60\%}$ gives us an estimate of the distribution of the dense molecular gas in the disc, while $H_{90\%}$ informs us about the envelope of the disc. Fig. 17 shows the time evolution of $H_{60\%}$

(top panel) and $H_{90\%}$ (bottom panel) for all the simulations. For the initial ~ 10 Myr, the disc cools and contracts reducing $H_{60\%}$ to ~ 10 pc and $H_{90\%}$ to ~ 20 pc. This gas compression leads to a starburst-induced outflow leading to an increase in both $H_{60\%}$ and $H_{90\%}$. The stronger outflows in the ESF runs cause $H_{90\%}$ to reach a peak of about ~ 600 pc at $t = 40$ Myr, while it only increases to about ~ 200 pc in the SN run. At the same time $H_{60\%}$ increases to ~ 200 pc in the ESF runs and ~ 60 pc in the SN run. Both heights decrease during the inflow period and then rebound back and remain fairly constant after $t > 75$ Myr. At these late times, the difference in $H_{90\%}$ between the SN (~ 150 pc) and ESF runs is quite nominal (~ 200 pc), with the ESF runs having a larger value by about 50%. $H_{60\%}$, on the other hand shows about a factor of two increase in the ESF (~ 60 pc) runs. This implies that the discs in ESF runs are more puffed up due to additional pressure from the photoheated gas, which in turn reduces the midplane pressure reducing the SFR.

It is also worth noting that the temperature and pressure difference between the SN and ESF runs in the high density star forming gas ($n_H \gtrsim 100$ cm $^{-3}$) is quite small, implying very little difference between the sites of star formation in the different runs. However, once the stars form, photoheating of high density material around a newly formed star, over-pressurises the region, which then expands till it reaches a pressure equilibrium with the surrounding gas. This reduces the density of the gas and causes a pileup of material at the photoheating temperature (about $\sim 10^4$ K for a soft spectra from

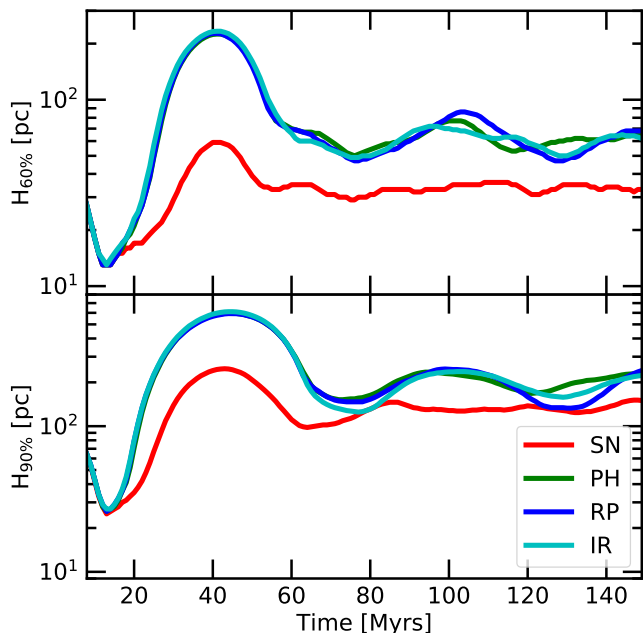


Figure 17. Vertical heights of 60% (top panel) and 90% enclosed mass as a function of time for the SN (red curves), PH (green curves), RP (blue curves) and IR (cyan curves) simulations. ESF increases the scale height of the disc almost a factor of ~ 2 .

stars), a prominent feature in the ESF runs. Direct evidence for this effect can be gained by looking at the mean densities at which the SNe explode in the different runs. Fig. 18 plots the cumulative distribution of the number of SNe as a function of the mean density at which they explode in the SN (red curve), PH (green curve), RP (blue curve) and IR (cyan curve) simulations. In SN run, about 50% of the SNe explode in star forming high density gas and about 90% in gas with $n > 10 \text{ cm}^{-3}$. Since the star formation density threshold is $n = 100 \text{ cm}^{-3}$, this means that the SNe in the SN run are rarely able to get out of their respective birth clouds. On the other hand, in the ESF runs, the more than 80% of the SNe explode in gas with $n < 10 \text{ cm}^{-3}$ and more than 90% in gas with $n < 100 \text{ cm}^{-3}$, implying that radiation fields reduce the mean ambient density by a factor of about 10 – 100.

The evolution of a SNe remnant in different density environments have been studied in great detail by many recent works (Kim & Ostriker 2015; Martizzi et al. 2015; Haid et al. 2016). Briefly, the evolution of the SNe can be divided into five phases (McKee & Ostriker 1977), the pre Sedov-Taylor (PST) phase, the Sedov-Taylor (ST) phase, the transition phase (TR), the pressure driven snowplough (PDS) phase and finally the momentum conserving (MC) phase. During the PST phase, the SNe ejecta runs into the ambient ISM shocking and thermalizing a large fraction of the injected energy. This then initiates an energy conserving ST phase, which ends when the rate-of-change of temperature due to adiabatic expansion is comparable to radiative losses. The expansion then transitions to a regime, where the adiabatic and radiative cooling contributes about equally called the transition phase. Finally, the PDS phase is defined by the domination of radiative cooling with the pressure inside the bubble driving the expansion of the SNe remnant. During all these evolutionary phases the increased thermal pressure within the bubble pushes on the surrounding low pressure ISM boosting the final momentum output of the SNe event. Eventually,

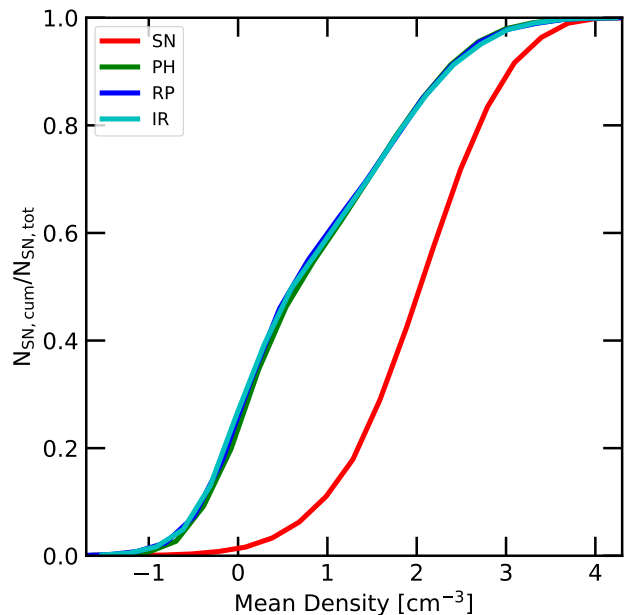


Figure 18. Normalised cumulative counts of the supernovae as a function of the mean environmental density in which they explode for the SN (red curves), PH (green curves), RP (blue curves) and IR (cyan curves) simulations. Photoheating reduces the density at which the SNe go off by a factor of 10 – 100, thereby increasing the momentum input of a SNe feedback event.

when the pressure inside the bubble becomes equal to the ambient pressure, the remnant becomes momentum-conserving. Simulations have shown that the momentum boost achieved in realistic ISM environments is about a factor of 13 – 30 depending on the ambient density in which the SNe explodes. The duration of the ST, TR and PDS phases depends on the cooling time of the gas, which in turn depends on the ambient density, with more cooling occurring in higher density gas ($t_{\text{cool}} \propto n^{-0.55}$). The longer cooling times in low density medium leads to a longer duration of the momentum boosting phases leading to more ISM material being swept up and accelerated to larger velocities, with the mass of the swept up material scaling with ambient density as $M_{\text{swept}} \propto n^{-0.26}$ which implies that a reduction in the ambient density by a factor of ~ 100 increases the mass of the swept material by about a factor of ~ 3 . Therefore, we can conclude that because SNe explode in lower density environments in the ESF simulations, the duration of the momentum boosting phases is longer, leading to a higher amount of the colder, denser ISM (compared to the hot wind) being swept up and accelerated to larger velocities in the outflow. This not only explains the increased mass and energy loading factors in the ESF runs, but also the increased entrainment of colder and denser gas.

Finally, we note that the resolved SNe momentum budget has only a weak dependence on the density of the ambient medium $\dot{p} \propto n^{-0.19}$ (Kim & Ostriker 2015; Martizzi et al. 2015; Haid et al. 2016). Using this scaling we can conclude that radiation fields can increase the momentum output of the SNe by a factor of about 1.5–2.5. This increased coupling efficiency combined with the fact that the radiation fields provide additional pressure support against gravity explains the differences between the SN and ESF runs presented in this paper. These effects are in agreement with previous

self-consistent RHD simulations presented in Rosdahl & Teyszier (2015) & Peters et al. (2017).

5 CONCLUSIONS

In this paper, we present extremely high resolution radiation hydrodynamic simulations of a small patch of the inter-stellar medium performed with AREPO-RT. We performed four simulations, SN: simulation with just SNe feedback, PH: SN + photoheating from local radiation fields, RP: PH + effect of UV radiation pressure and IR: RP + effect of multiscattering infrared radiation pressure. These simulations were performed with a mass resolution of $10 M_{\odot}$ and a spatial resolution of ~ 45 pc. This allows us to resolve all the relevant feedback processes, thereby providing us with an accurate picture of stellar feedback in low gas surface density galaxies. Our main results can be summarised as follows:

- Radiation fields have the effect of reducing the star formation rates and thereby the total stellar mass of the galaxies by about a factor of ~ 2 . This has the effect of increasing the gas depletion timescales in the simulations, thereby allowing for a better match with the observed Kennicutt-Schmidt relation.
- The most important effect of radiation fields is photoheating through UV photons. Radiation pressure both single and multiscattered, does not have a significant effect in low gas surface density environments.
- The mass and energy loading factors increase by $\sim 5 - 10$ in the presence of radiation fields. The increase is mainly driven by the additional entrainment of medium density ($10^{-2} \leq n < 1 \text{ cm}^{-3}$), warm ($300 \text{ K} \leq T < 8000 \text{ K}$) material in the outflow. This material has velocities of about $\sim 10 - 100 \text{ km s}^{-1}$, meaning that it falls back onto the disc creating a fountain flow of order ~ 2 kpc. Radiation fields, therefore, help drive colder, denser and higher mass and energy loaded outflows compared to models that invoke only SNe feedback.
- The radiation fields from stars generates an inter-stellar radiation field (ISRF) that permeates through the disc increasing the temperature of the gas which in turn increases the pressure support of the gas against gravitational collapse. This puffs up the disc and reduces star formation.
- Photoheating of high density material around a newly formed star over-pressurises the region, which then expands till reaches a pressure equilibrium with the surrounding gas. This reduces the ambient density in which the SNe explodes by a factor of $10 - 100$, increasing its momentum input by a factor of $\sim 1.5 - 2.5$.

The relatively high star formation rates even with radiation fields hint that there might be additional feedback mechanisms that have not been accounted for in our present work such as stellar winds (Gatto et al. 2017; Peters et al. 2017), binary stars (Kim & Ostriker 2017) or cosmic rays (Simpson et al. 2016; Ruzskowski et al. 2017; Diesing & Caprioli 2018). We plan to include the effect of all three processes in a future work.

The effect of radiation pressure is minimal when it acts together with photoheating, because the latter is substantially more efficient in inducing velocities comparable to the sound speed of the hot ionized medium on time-scales far shorter than required for accumulating similar momentum with radiation pressure. This allows photoheating to dominate the feedback as the heating and expansion of gas lowers the central densities, further diminishing the impact of radiation pressure (Sales et al. 2014). In the future, we plan to build upon this work and test the effect of radiation

pressure in high surface density, star-bursting galaxies (Kleinmann et al. 1988) as well as in more massive giant molecular clouds in low surface density galaxies, as this mechanism is theorised to be more effective in these environments (Hopkins et al. 2011; Thompson et al. 2015; Rahner et al. 2017).

Another caveat of this work is that the geometry of the tallbox setup is not realistic. Previous works have shown that the properties of galactic winds are not accurately predicted because they do not capture the correct global geometry and gravitational potential of galaxies (Martizzi et al. 2016). The wind mass and energy loading factors are not well-defined because they decline significantly with increasing box height. However, this local tallbox setup was required to achieve the resolution necessary to resolve relevant feedback processes in our simulations. We plan to run physically realistic calculations (e.g., isolated full disc simulation) to fully understand the role of radiation fields in launching galactic outflows in the future. While, we have only focused on the dynamical impact of early stellar feedback, radiation fields also change the chemical composition of the ISM which we will investigate in a future paper. We conclude by noting that early stellar feedback in the form of photoheating is an important physical process that enhances the effectiveness of SNe feedback, a result that is in agreement previous self-consistent RHD simulations (Rosdahl & Teyszier 2015; Gatto et al. 2017; Peters et al. 2017; Emerick et al. 2018), thereby confirming the important role that radiation fields play in regulating star formation and determining the structure of the ISM and outflows in galaxies.

ACKNOWLEDGEMENTS

RK acknowledges support from NASA through Einstein Postdoctoral Fellowship grant number PF7-180163 awarded by the *Chandra* X-ray Center, which is operated by the Smithsonian Astrophysical Observatory for NASA under contract NAS8-03060. SCOG acknowledges support from the Deutsche Forschungsgemeinschaft (DFG) via SFB 881 “The Milky Way System” (sub-projects B1, B2 and B8). Computing resources supporting this work were provided by the NASA High-End Computing (HEC) Program through the NASA Advanced Supercomputing (NAS) Division at Ames Research Center and by XSEDE project AST180025 via the Comet supercomputer center at San Diego.

REFERENCES

- Agertz O., Kravtsov A. V., Leitner S. N., Gnedin N. Y., 2013, *ApJ*, 770, 25
 Baczynski C., Glover S. C. O., Klessen R. S., 2015, *MNRAS*, 454, 380
 Bruzual G., Charlot S., 2003, *MNRAS*, 344, 1000
 Cantalupo S., 2010, *MNRAS*, 403, L16
 Chabrier G., 2003, *PASP*, 115, 763
 Creasey P., Theuns T., Bower R. G., 2013, *MNRAS*, 429, 1922
 Dalla Vecchia C., Schaye J., 2008, *MNRAS*, 387, 1431
 Davis S. W., Jiang Y.-F., Stone J. M., Murray N., 2014, *ApJ*, 796, 107
 Diesing R., Caprioli D., 2018, *Physical Review Letters*, 121, 091101
 Draine B. T., Bertoldi F., 1996, *ApJ*, 468, 269
 Emerick A., Bryan G. L., Mac Low M.-M., 2018, *ApJ*, 865, L22
 Fielding D., Quataert E., Martizzi D., Faucher-Giguère C.-A., 2017, *MNRAS*, 470, L39
 Gatto A., et al., 2017, *MNRAS*, 466, 1903
 Girichidis P., et al., 2016, *MNRAS*, 456, 3432
 Glover S. C. O., Clark P. C., 2012, *MNRAS*, 421, 116
 Glover S. C. O., Mac Low M.-M., 2007a, *ApJS*, 169, 239
 Glover S. C. O., Mac Low M.-M., 2007b, *ApJ*, 659, 1317

Gnat O., Ferland G. J., 2012, *ApJS*, 199, 20
 Gnedin N. Y., Draine B. T., 2014, *ApJ*, 795, 37
 Gnedin N. Y., Hollon N., 2012, *ApJS*, 202, 13
 Guedes J., Callegari S., Madau P., Mayer L., 2011, *ApJ*, 742, 76
 Haid S., Walch S., Naab T., Seifried D., Mackey J., Gatto A., 2016, *MNRAS*, 460, 2962
 Haiman Z., Abel T., Rees M. J., 2000, *ApJ*, 534, 11
 Hopkins P. F., Grudic M. Y., 2018, preprint, ([arXiv:1803.07573](https://arxiv.org/abs/1803.07573))
 Hopkins P. F., Quataert E., Murray N., 2011, *MNRAS*, 417, 950
 Hopkins P. F., Kereš D., Oñorbe J., Faucher-Giguère C.-A., Quataert E., Murray N., Bullock J. S., 2014, *MNRAS*, 445, 581
 Hopkins P. F., et al., 2017, preprint, ([arXiv:1702.06148](https://arxiv.org/abs/1702.06148))
 Kannan R., et al., 2014a, *MNRAS*, 437, 2882
 Kannan R., Stinson G. S., Macciò A. V., Brook C., Weinmann S. M., Wadsley J., Couchman H. M. P., 2014b, *MNRAS*, 437, 3529
 Kannan R., Vogelsberger M., Stinson G. S., Hennawi J. F., Marinacci F., Springel V., Macciò A. V., 2016, *MNRAS*, 458, 2516
 Kannan R., Vogelsberger M., Marinacci F., McKinnon R., Pakmor R., Springel V., 2018, preprint, ([arXiv:1804.01987](https://arxiv.org/abs/1804.01987))
 Katz N., Weinberg D. H., Hernquist L., 1996, *ApJS*, 105, 19
 Kennicutt Jr. R. C., 1998, *ApJ*, 498, 541
 Kennicutt R. C., Evans N. J., 2012, *ARA&A*, 50, 531
 Kim C.-G., Ostriker E. C., 2015, *ApJ*, 802, 99
 Kim C.-G., Ostriker E. C., 2017, *ApJ*, 846, 133
 Kleinmann S. G., Hamilton D., Keel W. C., Wynn-Williams C. G., Eales S. A., Becklin E. E., Kuntz K. D., 1988, *ApJ*, 328, 161
 Krumholz M. R., Thompson T. A., 2013, *MNRAS*, 434, 2329
 Leitherer C., et al., 1999, *ApJS*, 123, 3
 Leroy A. K., Walter F., Brinks E., Bigiel F., de Blok W. J. G., Madore B., Thornley M. D., 2008, *AJ*, 136, 2782
 Machacek M. E., Bryan G. L., Abel T., 2001, *ApJ*, 548, 509
 Marinacci F., et al., 2018, *MNRAS*, 480, 5113
 Martizzi D., Faucher-Giguère C.-A., Quataert E., 2015, *MNRAS*, 450, 504
 Martizzi D., Fielding D., Faucher-Giguère C.-A., Quataert E., 2016, *MNRAS*, 459, 2311
 McKee C. F., Ostriker J. P., 1977, *ApJ*, 218, 148
 Muratov A. L., Kereš D., Faucher-Giguère C.-A., Hopkins P. F., Quataert E., Murray N., 2015, *MNRAS*, 454, 2691
 Murray N., Quataert E., Thompson T. A., 2010, *ApJ*, 709, 191
 Naiman J. P., et al., 2018, *MNRAS*, 477, 1206
 Navarro J. F., Frenk C. S., White S. D. M., 1996, *ApJ*, 462, 563
 Nelson R. P., Langer W. D., 1997, *ApJ*, 482, 796
 Nelson D., et al., 2018, *MNRAS*, 475, 624
 Nickerson S., Teyssier R., Rosdahl J., 2018, *MNRAS*, 479, 3206
 Oppenheimer B. D., Davé R., 2006, *MNRAS*, 373, 1265
 Pakmor R., Springel V., Bauer A., Mocz P., Munoz D. J., Ohlmann S. T., Schaal K., Zhu C., 2016, *MNRAS*, 455, 1134
 Peters T., et al., 2017, *MNRAS*, 466, 3293
 Pillepich A., et al., 2018, *MNRAS*, 475, 648
 Rahner D., Pellegrini E. W., Glover S. C. O., Klessen R. S., 2017, *MNRAS*, 470, 4453
 Rosdahl J., Teyssier R., 2015, *MNRAS*, 449, 4380
 Rosdahl J., Schaye J., Teyssier R., Agertz O., 2015, *MNRAS*, 451, 34
 Roškar R., Teyssier R., Agertz O., Wetzstein M., Moore B., 2014, *MNRAS*, 444, 2837
 Ruzkowski M., Yang H.-Y. K., Zweibel E., 2017, *ApJ*, 834, 208
 Sales L. V., Marinacci F., Springel V., Petkova M., 2014, *MNRAS*, 439, 2990
 Schaye J., et al., 2015, *MNRAS*, 446, 521
 Simpson C. M., Bryan G. L., Hummels C., Ostriker J. P., 2015, *ApJ*, 809, 69
 Simpson C. M., Pakmor R., Marinacci F., Pfrommer C., Springel V., Glover S. C. O., Clark P. C., Smith R. J., 2016, *ApJ*, 827, L29
 Smith M. C., et al., 2007, *MNRAS*, 379, 755
 Smith R. J., Glover S. C. O., Clark P. C., Klessen R. S., Springel V., 2014, *MNRAS*, 441, 1628
 Somerville R. S., Davé R., 2015, *ARA&A*, 53, 51
 Springel V., 2010, *MNRAS*, 401, 791

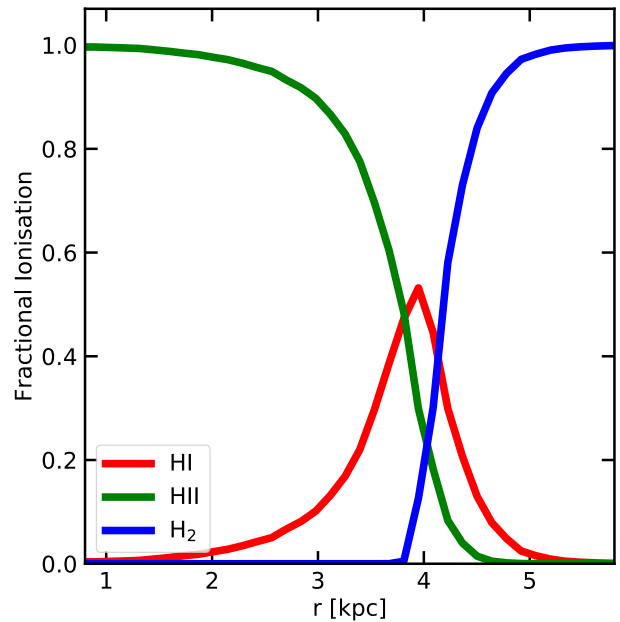


Figure A1. Profiles of the neutral hydrogen (red curve), ionized hydrogen (green curve) and molecular hydrogen (blue curve) fractions as a function of radius around an O star at the end of the molecular Strömgren sphere test.

Springel V., Hernquist L., 2003, *MNRAS*, 339, 289
 Springel V., et al., 2018, *MNRAS*, 475, 676
 Sternberg A., Le Petit F., Roueff E., Le Bourlot J., 2014, *ApJ*, 790, 10
 Stinson G., Seth A., Katz N., Wadsley J., Governato F., Quinn T., 2006, *MNRAS*, 373, 1074
 Stinson G. S., Brook C., Macciò A. V., Wadsley J., Quinn T. R., Couchman H. M. P., 2013, *MNRAS*, 428, 129
 Thacker R. J., Couchman H. M. P., 2001, *ApJ*, 555, L17
 Thompson T. A., Fabian A. C., Quataert E., Murray N., 2015, *MNRAS*, 449, 147
 Vogelsberger M., Genel S., Sijacki D., Torrey P., Springel V., Hernquist L., 2013, *MNRAS*, 436, 3031
 Vogelsberger M., et al., 2014a, *MNRAS*, 444, 1518
 Vogelsberger M., et al., 2014b, *Nature*, 509, 177
 Walch S., Naab T., 2015, *MNRAS*, 451, 2757
 Walch S. K., Whitworth A. P., Bisbas T., Wünsch R., Hubber D., 2012, *MNRAS*, 427, 625
 Zhang D., Davis S. W., 2017, *ApJ*, 839, 54
 Kleinmann1988

APPENDIX A: H₂ THERMOCHEMISTRY

As a test for our H₂ thermochemistry we perform a Strömgren sphere test in a molecular medium (Nickerson et al. 2018, Section 3.4). We start with a completely molecular solar-metallicity gas at a density of $n_H = 10^{-3} \text{ cm}^{-3}$ and a temperature of $13.56 \times 10^3 \text{ K}$. The simulation box has a side of length 15 kpc which is resolved by 32^3 resolution elements. We do not include any photoheating or cooling effects. The central ionization source is a O star which emits radiation spectrum equivalent to a blackbody with an effective temperature of $4.3 \times 10^4 \text{ K}$. Three frequency bins used in this test are, the Lyman-Werner (LW; H₂ dissociation) band (11.2 – 13.6 eV), hydrogen ionization band (13.6 – 15.2 eV) and H I and H₂ ionization band (15.2 – 24.6 eV). The total lu-

minosity is set such that the number of H_2 dissociation photons $\dot{N}_{H_2} = 3 \times 10^{48} \text{ s}^{-1}$ and the number of $H\text{ I}$ ionization photons is $\dot{N}_{HI} = 5 \times 10^{48} \text{ s}^{-1}$. The H_2 ionization rates are taken from [Baczynski et al. \(2015\)](#) and the H_2 dissociation rates and the self-shielding prescriptions are obtained from [Nickerson et al. \(2018\)](#). For these conditions the radius of the Strömgren sphere is

$$r_{s,HI} = \left(\frac{3\dot{N}_{HI}}{4\pi\alpha_{HI}n_H^2} \right)^{1/3} \sim 4.1 \text{ kpc}, \quad (\text{A1})$$

where α_{HI} is the Case B recombination rate.

Fig. A1 shows the fractional ionization profiles of molecular (blue curve), neutral (red curve) and ionized (green curve) hydrogen after 500 Myr of evolution. The $H\text{ II}$ region ends sharply at 4.1 kpc as expected. The self-shielding prescription is able to block most of the LW photons from entering into the molecular layer producing a relatively sharp and thin $H\text{ I}$ layer between the fully ionized $H\text{ II}$ and fully molecular H_2 layers. This nicely matches with the results obtained by [Nickerson et al. \(2018\)](#), thereby confirming the accuracy of our scheme.

This paper has been typeset from a $\text{\TeX}/\text{\LaTeX}$ file prepared by the author.